

Modeling Wind-Induced Changes to Overturning Wave Shape

Falk Feddersen¹†, Kentaro Hanson², Wouter Mostert³, Adam Fincham^{4,5}

¹ Scripps Institution of Oceanography, UCSD, La Jolla, CA, USA

² Program in Applied and Computational Mathematics, Princeton University, Princeton NJ, USA

³ Department of Engineering Science, Oxford University, UK.

⁴ Kelly Slater Wave Company, Los Angeles, CA, USA

⁵ Department of Aerospace and Mechanical Engineering, University of Southern California, Los Angeles, CA

(Received xx; revised xx; accepted xx)

Depth-limited overturning wave shape affects water turbulence and sediment suspension. Experiments have shown that wind affects shoaling and overturning wave shape, with uncertain mechanism. Here we study wind effects (given by wind Reynolds number) on solitary wave shoaling and overturning with the 2-phase DNS model Basilisk run in two-dimensions on steep bathymetry for a fixed wave Reynolds and Bond number. For all wind, the propagating solitary wave sheds a 2D turbulent air wake and has nearly uniform speed with minimal wave energy changes over the rapidly varying bathymetry. Wave-face slope is influenced by wind, and shoaling wave shape changes are consistent with previous studies. As overturning jet impacts, wind-dependent differences in overturn shape are quantified. The nondimensional breakpoint location and overturn area have similar wind dependence as experiment, albeit requiring larger wind speed. The overturn aspect ratio has opposite wind dependence as experiment. During shoaling, the surface viscous stresses are negligible relative to pressure. Surface tension effects are also small but grow rapidly near overturning. In a wave frame of reference, surface pressure is low in the lee and contributes 2-5% to the velocity potential rate of change in the surface dynamic boundary condition, which, integrated over time, changes the wave shape. Reasons the overturn aspect ratio is different than experiment and why a stronger simulated wind is required are explored. The dramatic wind-effects on overturning jet area, and thus to the available overturn potential energy, make concrete the implications of wind-induced changes to wave shape.

1. Introduction

As they approach shore, shoaling waves change shape becoming steeper with narrower peaks and more pitched forward (e.g. Elgar & Guza 1985). Once sufficiently steepened, depth-limited wave breaking occurs with wave overturning, and subsequently the overturn jet impacts the water-surface in front of the wave. Depth-limited wave breaking is often qualitatively categorized into spilling and plunging (e.g. Peregrine 1983), where spilling waves have very small overturns and plunging waves have larger overturns. Bathymetry along with offshore wave height and wavelength are well understood (e.g. via the Iribarren number) to be important in setting spilling or plunging wave breaking (e.g. Peregrine 1983). For example, larger planar beach slope β leads to larger overturns (Grilli *et al.* 1997; Mostert & Deike 2020; O’Dea *et al.* 2021). Across laboratory and field observations, the wave overturn shape is important in the resulting splash up and bubble entrainment (Chanson & Jaw-Fang 1997; Yasuda *et al.* 1999; Blenkinsopp & Chaplin 2007), water column turbulence (Ting & Kirby 1995, 1996; Aagaard *et al.* 2018), sediment suspension

† Email address for correspondence: ffeddersen@ucsd.edu

(e.g. Aagaard *et al.* 2018), and wave impact forces on engineered structures (Bullock *et al.* 2007). Similarly in numerical simulations of deep-water and depth-limited wave breaking, the geometry of wave overturning impacts air entrainment, vorticity generation, and pathways of turbulent dissipation (e.g. Lubin *et al.* 2006; Derakhti & Kirby 2014; Mostert *et al.* 2022). Thus, understanding the factors that affect the shape of overturning waves is important to a range of processes.

In deep water, wind is well understood to lead to surface gravity wave growth and decay (e.g. Miles 1957; Phillips 1957). However, wind can also change wave shape in both deep (Leykin *et al.* 1995; Zdyrski & Feddersen 2020) and shallow (Zdyrski & Feddersen 2021) water, as well as in shoaling waves (Feddersen & Veron 2005; Sous *et al.* 2021; Zdyrski & Feddersen 2022). In laboratory studies, onshore wind results in wave breaking in deeper water (farther offshore) (Douglass 1990; Sous *et al.* 2021), with the opposite for offshore wind. Feddersen *et al.* (2023) studied the explicit wind dependence of overturn wave shape at the Surf Ranch, a wave basin designed for surfing. Field-scale shoaling solitary wave with height ≈ 2.25 m propagated at $C = 6.7$ m s⁻¹ and overturned. The cross-wave component of wind U , measured 16 m above the water surface, varied from onshore to offshore with realistic $-1.2 < U/C < 0.7$. The non-dimensionalized breakpoint location was inversely related to U/C , consistent with Douglass (1990). The nondimensional overturn area A/H_b^2 , where H_b is breaking wave height, and overturn aspect ratio (overturn width divided by length) were also inversely related to U/C , with smaller area and overturns for increasing onshore wind (positive U/C). For increasing offshore wind, A/H_b^2 was approximately uniform. The nondimensional overturn parameters varied by a factor of two for the observed U/C indicating that the wind has a significant effect on overturn shape. However, the mechanism by which wind induces these geometric changes is uncertain. For example, the pressure profiles induced by the wind on the different parts of the evolving wave, along with the general flow structure over and around the wave, remain unknown.

Numerical modeling offers a promising avenue for investigating wind effects on shoaling and overturning wave shape. For over two decades, volume of fluid (VOF) based numerical models have enabled the study of various aspects of wave breaking (e.g. Lin & Liu 1998; Chen *et al.* 1999; Guignard *et al.* 2001). More recent advances in two phase numerical modeling both DNS and LES has enabled significant advances in understanding aspects of deep (Lubin *et al.* 2019; Mostert *et al.* 2022) and shallow water wave breaking (e.g. Lubin & Glockner 2015; Mostert & Deike 2020; Boswell *et al.* 2023; Liu *et al.* 2023). Similar advances have occurred in the study of wind input of energy and momentum to deep water waves with coupled (e.g. Hao & Shen 2019) and VOF (Wu *et al.* 2022) models. Numerical studies using two-dimensional (2D) two-phase RANS solvers of wind-forced solitary (Xie 2014) and progressive (Xie 2017) waves have seen a wind-induced shift in breakpoint location analogous to laboratory experiments. Analogous wind effects were seen in 2D LES simulations of deep water wave breaking (Chen & Zou 2022). However, the effect of wind on shoaling and overturning waves has not been in detail studied with numerical models.

Here, we study the wind effects on solitary wave shoaling and overturning for a model domain similar to that of Feddersen *et al.* (2023) using the two-phase numerical model Basilisk run in 2D up until the moment the overturning jet impacts. The breaking processes that occur after jet impact have been and are actively being studied with numerical models (e.g. Lin & Liu 1998; Mostert & Deike 2020; Boswell *et al.* 2023; Liu *et al.* 2023; Chen *et al.* 2024). In section 2, the model setup is described, the key nondimensional parameters including wind Reynolds number Re^* are defined, and the relationship between modeled air velocity $\langle \bar{U} \rangle / C$ and Re^* is discussed. In Section 3.1, the qualitative features of the shoaling solitary wave and air vorticity are examined for strong onshore and offshore wind. The statistics of solitary wave shoaling under strong onshore and offshore wind are described in section 3.2. Overturn wave shape is quantified by geometrical parameters defined at the moment of jet impact (Section 3.3). The relationship of the nondimensional geometrical parameters (defined in Section 3.4) to Re^* is examined (Section 3.5). The relative strength of

viscous stresses and pressure at the air-water interface is examined in Section 3.6, and the terms of the surface dynamic boundary condition including pressure variations and surface tension are analyzed in Section 3.7. We discuss the shoaling results relative to previous studies, examine potential reasons for the differences between our results here and those of field-scale experiments, and consider implications in Section 4. Section 5 provides a summary.

2. Methods

We numerically simulate in two dimensions (2D) the shoaling and overturning of a solitary wave with the two-phase incompressible Navier-Stokes equations using the open-source Basilisk software package (Popinet 2003, 2009, 2018) for solving partial differential equations on an adaptively refined grid. Basilisk has been extensively used to model wave breaking (Deike *et al.* 2015, 2016; Mostert & Deike 2020; Mostert *et al.* 2022), as well as wave interactions with wind (Wu & Deike 2021; Wu *et al.* 2022).

2.1. Formulation and Governing Equations

The governing equations are the two-phase (water and air) Navier-Stokes equations in 2D, given as

$$\begin{aligned} \frac{\partial \rho}{\partial t} + \nabla \cdot (\rho \mathbf{u}) &= 0 \\ \rho \left(\frac{\partial \mathbf{u}}{\partial t} + \mathbf{u} \cdot \nabla \mathbf{u} \right) &= -\nabla p + \rho \mathbf{g} + \nabla \cdot (2\mu \mathbf{D}) + \sigma \kappa \mathbf{n} \delta_s \\ \nabla \cdot \mathbf{u} &= 0 \end{aligned} \quad (2.1)$$

where \mathbf{u} , σ , κ , \mathbf{D} , \mathbf{g} are the fluid velocity, surface tension, curvature of the interface, deformation tensor, and acceleration due to gravity, respectively. In component form, the 2D fluid velocity $\mathbf{u} = (u, w)$ where u and w are the horizontal and vertical velocities, respectively. For each fluid, the water and air density (ρ_w, ρ_a) and dynamic viscosity (μ_w, μ_a) are uniform. A volume-of-fluid (VOF) advection scheme with a color function f is used to capture and advect the air-water interface in a momentum-conserving implementation. Hence for two-phase mixtures, ρ and μ are represented by

$$\begin{aligned} \rho &= f \rho_w + (1 - f) \rho_a \\ \mu &= f \mu_w + (1 - f) \mu_a \end{aligned} \quad (2.2)$$

where f is interpreted as the liquid volume fraction ($f = 1$ for water, $f = 0$ for air). The water-to-air ratio for ρ and μ are important nondimensional parameters and are here held fixed at $\rho_a/\rho_w = 0.001$ and $\mu_a/\mu_w = 0.018$. The air-water interface requires continuity of velocity and stress, including surface tension. Surface tension as the interfacial force $\sigma \kappa \mathbf{n} \delta_s$ is determined from the Dirac delta δ_s on the interface and the unit normal vector \mathbf{n} . This formulation is expressed in Popinet (2018), alongside the implementation of gravity as an interfacial force. In (2.1), we substitute

$$\rho \mathbf{g} \rightarrow (\rho_a - \rho_w)(\mathbf{g} \cdot \mathbf{x}) \mathbf{n} \delta_s$$

which are equal, up to a difference in the pressure field. The reduced gravity implementation avoids the appearance of spurious velocities and unphysical energy production near the air-water interface (Wroniszewski *et al.* 2014).

The two phase incompressible Navier-Stokes equations are solved on an adaptive Cartesian mesh using the Bell-Colella-Glaz projection method (Bell *et al.* 1989) with the VOF scheme described above, allowing for a sharp interface between phases (Fuster & Popinet 2018; López-Herrera *et al.* 2019; van Hooft *et al.* 2018). The bathymetry is represented with an additional volume fraction

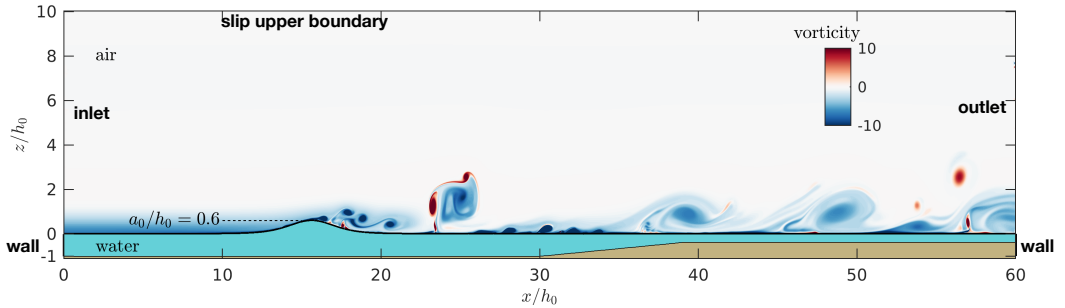


Figure 1. The simulation domain just after initialization as a function of nondimensional horizontal x/h_0 and vertical z/h_0 coordinates. The brown region represents the bathymetry, the aqua blue is water, the air-sea interface is indicated by the black curve, and air vorticity is given by the colorbar. The deeper flat water depth at $x/h_0 < 30$ has depth h_0 such that the bed is located at $z/h_0 = -1$. The shallow flat region has depth $h_s/h_0 = 0.371$, and the bathymetric slope connecting these two regions has slope $\beta = 0.0693$. The solitary wave initial condition parameters are $a_0/h_0 = 0.6$ and $x_0/h_0 = 15$. The height of the air domain is $h_a/h_0 = 10$. This example is for onshore wind and $Re^* = 2400$. The air inlet and outlet boundary conditions, together with the slip upper boundary condition are noted. The air vorticity is from the initial condition derived from the air-only precursor simulation.

120 field as an embedded boundary (Johansen & Colella 1998). Surface tension is implemented using
 121 the continuum-surface-force approach due to Brackbill *et al.* (1992).

122 2.1.1. Model Domain and Boundary Conditions

123 The model domain (figure 1) is similar to that used in Boswell *et al.* (2023) with modifications
 124 to be analogous to the bathymetry of the Surf Ranch (Feddersen *et al.* 2023). In the offshore region,
 125 the bathymetry is flat with depth h_0 and the total cross-shore (x) domain size is $L_x = 60h_0$. The
 126 offshore flat bathymetry extends for a x/h_0 -distance of 30. At $x/h_0 = 30$, the bathymetry slopes
 127 upward with a slope of $\beta = 0.0693$ over a x/h_0 -distance of 9.08 to a shallow depth $h_s/h_0 = 0.371$,
 128 which then extends a x/h_0 -distance of nearly 20. The bathymetric slope is a key non-dimensional
 129 parameter well understood to affect overturn shape (e.g. Grilli *et al.* 1997; Mostert & Deike
 130 2020; O’Dea *et al.* 2021). Here, β is held fixed to the Surf Ranch bathymetric slope projected in
 131 the direction of wave propagation (Feddersen *et al.* 2023) in order to isolate the wind-effects on
 132 overturning shape. The bathymetry has a no-slip boundary condition for fluid velocity. At the ends
 133 of the model domain at $x = 0$ and $x/h_0 = 60$, vertical walls extend from the bathymetry to the still
 134 water depth at $z/h_0 = 0$, with associated $u = 0$ and no-slip boundary conditions. The air domain
 135 extends vertically from the water surface (mostly near $z/h_0 = 0$) to $z/h_0 = h_a/h_0 = 10$, where
 136 a “ceiling”, with a free-slip boundary condition, is placed on the domain (figure 1). Between
 137 $0 < z/h_0 < 10$, at the left and right boundaries ($x/h_0 = 0$ and $x/h_0 = 60$, figure 1) open boundaries
 138 allow for air flow in and out of the domain. The inlet and outlet locations vary depending on the
 139 wind direction. For onshore winds, the left side is the inlet and for offshore winds, the right side is
 140 the inlet. A Neumann condition is placed on the dynamic pressure, $\partial p/\partial x = 0$, on the inlet, and a
 141 Dirichlet dynamic pressure condition $p = 0$ is placed on the outlet, both uniformly in the vertical.

142 2.1.2. Water Solitary Wave Initial Condition and Wave-related Nondimensional Parameters

143 For simplicity, the solitary wave solution to the Green-Naghdi (GN) equations (Green *et al.*
 144 1974; Le Métayer *et al.* 2010) is chosen as an initial condition. The simulation free surface initial

145 condition η_0 is

$$\eta_0(x) = a_0 \operatorname{sech}^2 \left(\frac{(x - x_0)}{h_0} \left(\frac{3a_0/h_0}{4(1 + a_0/h_0)} \right)^{1/2} \right), \quad (2.3)$$

146 and the associated water velocity initial condition is,

$$u(x) = \frac{C\eta(x)}{h_0 + \eta(x)} \quad (2.4)$$

$$w(x, z) = C \frac{z + h_0}{h_0 + \eta(x)} \left(\frac{\partial \eta}{\partial x}(x) \right) \left(1 - \frac{\eta(x)}{h_0 + \eta(x)} \right),$$

147 where $C = \sqrt{(gh_0)(1 + a_0/h_0)}$ is the solitary wave propagation speed, and the vertical velocity is
 148 derived from continuity. The GN equations are fully nonlinear and weakly dispersive and are
 149 essentially equivalent to the fully nonlinear weakly dispersive Boussinesq equations of Wei *et al.*
 150 (1995). This solitary wave solution is similar to that of the KdV equation (e.g. Ablowitz 2011)
 151 with a small change making the soliton shape narrower. For all simulations, the non-dimensional
 152 solitary wave amplitude is set similar to that generated at the Surf Ranch (Feddersen *et al.* 2023)
 153 at $a_0/h_0 = 0.6$ and the center of the solitary wave is located at $x_0/h_0 = 15$ (figure 1), implying
 154 a non-dimensional propagation speed $\tilde{C} = C/\sqrt{gh_0} = 1.265$. Once the simulation starts, the
 155 solitary wave propagates in the $+x$ direction with speed close to \tilde{C} and adjusts, as the GN-based
 156 initial condition (2.3 & 2.4) is not an exact solution of the two-phase Navier-Stokes equations.
 157 The adjustment leads to the solitary wave becoming narrower and slightly taller as minor trailing
 158 transients are shed. For smaller $a_0/h_0 = 0.3$, analogous adjustment to the GN-based initial
 159 condition was seen, albeit with opposite sign, in Mostert & Deike (2020). The adjusted solitary
 160 wave is essentially identical across all simulations with different wind speeds, allowing examination
 161 of the wind effect on shoaling and overturning. The GN-equations are still approximate (Wei *et al.*
 162 1995), and using a fully nonlinear potential flow soliton solution (Tanaka 1986) likely would have
 163 reduced the adjustment to the initial condition. The solitary wave then shoals over the rapidly
 164 varying bathymetry and eventually overturns in the shallow flat region (figure 1).

165 From the initial condition solitary wave parameters, a wave Reynolds number is defined as
 166 (Mostert & Deike 2020; Boswell *et al.* 2023)

$$\operatorname{Re}_w = \frac{\sqrt{gh_0^3}}{\nu_w} \quad (2.5)$$

167 where $\nu_w = \mu_w/\rho_w$ is the kinematic viscosity of water, and the linear shallow water phase
 168 speed $\sqrt{gh_0}$ and offshore depth h_0 are used as velocity and length-scales. Here, as in previous
 169 studies (Mostert & Deike 2020; Boswell *et al.* 2023), we keep the wave Reynolds number fixed at
 170 $\operatorname{Re}_w = 4 \times 10^4$. The Bond number Bo is also an important nondimensional parameter tracking the
 171 importance of surface tension. For a solitary wave, Bo is defined as (Mostert & Deike 2020),

$$\operatorname{Bo} = \frac{(\rho_w - \rho_a)gh_0^2}{\sigma} \quad (2.6)$$

172 where h_0 is chosen as the length-scale because solitary wave width scales with the water depth
 173 (2.3). Here, we have a fixed $\operatorname{Bo} = 4000$ slightly larger than the $\operatorname{Bo} = 1000$ used in previous
 174 shoaling and breaking solitary wave studies (Mostert & Deike 2020; Boswell *et al.* 2023). A
 175 nondimensional time is defined as

$$\tilde{t} = \left(\frac{g}{h_0} \right)^{1/2} t, \quad (2.7)$$

176 with $\tilde{t} = 0$ defined at moment when the solitary wave begins propagating. Variables with a tilde

177 denote nondimensional variables. Our model setup is analogous to the VOF model without
 178 atmosphere of Guignard *et al.* (2001) whose solutions for an initial higher-order soliton (Tanaka
 179 1986) of $a_0/h_0 = 0.45$ were similar to the potential flow solutions from a highly-accurate boundary
 180 element model (Grilli *et al.* 1997).

181 2.1.3. Air Initial Condition

182 All shoaling and overturning solitary wave simulations require an airflow initial condition. This
 183 is defined by first running an air-phase-only precursor simulation (described in more detail in
 184 Appendix A) analogous to Wu *et al.* (2022). The precursor simulation solves for the airflow over
 185 a solitary wave in a reference frame of a constant solitary wave speed, with no-slip boundary
 186 conditions at the wave surface matching the solitary wave fluid velocity (2.4). This choice of
 187 boundary conditions at the wave surface in the precursor simulation ensures that, at the beginning
 188 of the two-phase shoaling simulation, the air-phase velocity field is consistent with the water
 189 velocity of the moving solitary wave. To force the wind, the air-only simulation has an external,
 190 spatially and temporally uniform pressure gradient applied, specified by a nominal friction velocity
 191 u_*

$$\frac{\partial p}{\partial x} = \frac{\rho_a u_* |u_*|}{h_a}. \quad (2.8)$$

192 We characterize the airflow with a wind Reynolds number (Wu *et al.* 2022)

$$\text{Re}^* = \frac{u_* h_a}{\nu_a}, \quad (2.9)$$

193 where ν_a is the kinematic viscosity of air and $h_a/h_0 = 10$ is the thickness of the undisturbed air
 194 layer. For offshore winds (air flow opposite of solitary wave propagation direction), u_* is negative
 195 as is the resulting Re^* . The velocity field in the air phase at the conclusion of the precursor
 196 simulation is then used as the initial condition for the shoaling wave problem, which solves the
 197 full two-phase system in a fixed reference frame. During the two-phase simulations, the forcing
 198 pressure gradient discussed above is removed. As the solitary wave fully overturns for all Re^* by
 199 $\tilde{t} = 21$, the wind does not have sufficient time to meaningfully decelerate (Appendix B).

200 2.1.4. Recapitulation of Nondimensional Parameters

201 The simulations are performed in nondimensional variables and coordinates. Most of the
 202 nondimensional parameters are held fixed and key fixed parameters are recapitulated here. The
 203 air-water density ratio is $\rho_a/\rho_w = 0.001$. The air-water dynamic viscosity ratio is $\mu_a/\mu_w = 0.018$.
 204 The initial solitary wave amplitude is $a_0/h_0 = 0.6$ corresponding to a wave Reynolds number
 205 of $\text{Re}_w = 4 \times 10^4$. The beach slope is $\beta = 0.0693$. Note, for a kinematic viscosity of water
 206 $\nu_w = 10^{-6} \text{ m}^2 \text{ s}^{-1}$, the wave Reynolds number implies a $h_0 = 0.055 \text{ m}$, a solitary wave amplitude
 207 of $a_0 = 0.033 \text{ m}$, and a solitary wave speed of $C = 0.93 \text{ m s}^{-1}$. For the field scale solitary waves
 208 at the Surf Ranch (Feddersen *et al.* 2023), the equivalent $\text{Re}_w = 1.4 \times 10^7$. Here, the $\text{Bo} = 4000$
 209 is four times larger than that previously in shoaling and breaking solitary wave studies (Mostert
 210 & Deike 2020; Boswell *et al.* 2023). We note that the Bond number for the field scale solitary
 211 waves at the Surf Ranch is $\text{Bo} = 3.6 \times 10^5$, almost a factor $100\times$ larger than used here. Thus, the
 212 present simulations are not at field scale with respect to viscous effects or surface tension effects,
 213 which will be explored in the Discussion. The nondimensional wind friction velocity Re^* (2.9)
 214 is hypothesized to be important in setting wind effects on overturning shape and is varied over
 215 $\text{Re}^* = \{-1800, -1200, -600, 0, 600, 1200, 1800, 2400\}$.

216 2.1.5. Adaptive Mesh Refinement and Convergence

217 Basilisk uses adaptive mesh refinement (AMR) to reduce computational cost. Refinement is
 218 based on the error of the velocity, VOF field, and solid boundary approximation, using a wavelet

219 estimation algorithm. The AMR approach used in Basilisk is described in van Hooff *et al.* (2018)
 220 . The Basilisk domain is a $L_x/h_0 \times L_x/h_0$ square, with quadtree subdivision, ensuring that all
 221 grid cells are square. A maximum of 14 levels of refinement was chosen so that the effective
 222 minimum mesh size becomes $\Delta x/h_0 = (L_0/h_0)/2^{14} = 3.7 \times 10^{-3}$, corresponding to a minimum
 223 dimensional mesh size of 0.2 mm, for a dimensional depth of $h_0 = 0.055$ m. Although the domain
 224 is a square, the vertical domain of interest is about 1/6 of the total vertical domain. The bathymetry
 225 is embedded as a bottom boundary condition within the domain, and the domain below the
 226 bathymetry remains essentially unresolved reducing computational cost.

227 Previous studies with Basilisk of breaking solitary waves (Mostert & Deike 2020; Boswell *et al.*
 228 2023) found that for waves as large as those here, grid convergence was ensured pre- and post-wave
 229 breaking regimes for resolution at $\Delta x/h_0 = 6 \times 10^{-3}$. The present resolution of $\Delta x/h_0 = 3.7 \times 10^{-3}$
 230 is thus more than sufficient for grid-convergence, ensuring that numerical dissipation does not
 231 affect the dynamics of the wave. Here, we are only interested in the model solutions up until the
 232 point that the overturning jet impacts the water surface in front of it, that is pre-breaking. In terms
 233 of refinement, the pre-breaking regime is much less demanding. As in figure 1, the scales of the 2D
 234 wind turbulence are not small. Therefore with 14 levels of refinement, the pre-breaking solution is
 235 expected to be converged.

236 2.1.6. Model output

237 Model output is stored every $\Delta \tilde{t} = 0.05$ for $\tilde{t} < 18$ and every $\Delta \tilde{t} = 0.01$ for $\tilde{t} \geq 18$ to ensure
 238 that the wave overturn is temporally well-resolved in the model output. From model output, fluid
 239 volume fraction f , velocity, vorticity, pressure are estimated on a regular grid over the domain. In
 240 addition, the air-water interface η , as well as interface velocities are output at the AMR resolution.
 241 Pressure at the interface can be noisy due to the surface tension term. Thus interface air pressure
 242 is estimated in the air, a distance $\Delta = 0.01$ normal to the surface interface. This distance is
 243 approximately $2.7 \times$ the minimum grid resolution at 14 levels of refinement. In addition we also
 244 output u and w in the air on a diamond stencil centered on the location of pressure with stencil
 245 leg distance 0.004 that allow 2nd order estimates of $\partial u/\partial x$, $\partial u/\partial z$, $\partial w/\partial x$ and $\partial w/\partial z$ over a
 246 separation of 0.008. As the wave propagates and shoals, most of the time the air-water interface η
 247 is single-valued with x/h_0 . Once the overturning jet forms, η is no longer single valued. For the
 248 times when single-valued, we define $\eta(x, t)$ as the air-water interface. Nondimensional water and
 249 air kinetic (K_w, K_a) and potential (P_w, P_a) energies are estimated as (e.g. Mostert *et al.* 2022)

$$250 \quad K_{w,a} = \int_{V_{w,a}} \frac{\rho}{2} |\mathbf{u}|^2 dV, \quad P_{w,a} = \int_{V_{w,a}} \rho g z dV. \quad (2.10)$$

250 where the integrals are over the water or air regions, respectively. The potential energy is referenced
 251 relative to the potential energy at $t = 0$. The water and air energy (kinetic plus potential) is thus

$$252 \quad E_{w,a}(t) = K_{w,a}(t) + [P_{w,a}(t) - P_{w,a}(0)] \quad (2.11)$$

252 Nondimensional water energy \tilde{E}_w is then given by

$$\tilde{E}_w = \frac{E_w}{\rho_w g h_0^3}. \quad (2.12)$$

253 2.2. Relationship between wind speed and wind Reynolds number Re^*

254 Before describing the evolution of the shoaling and overturning solitary wave under the effect
 255 of varying wind, we examine the dependence of model air velocity (wind) to Re^* . We will average
 256 the air velocity to have a single wind metric to compare with Re^* . The first averaging operator is

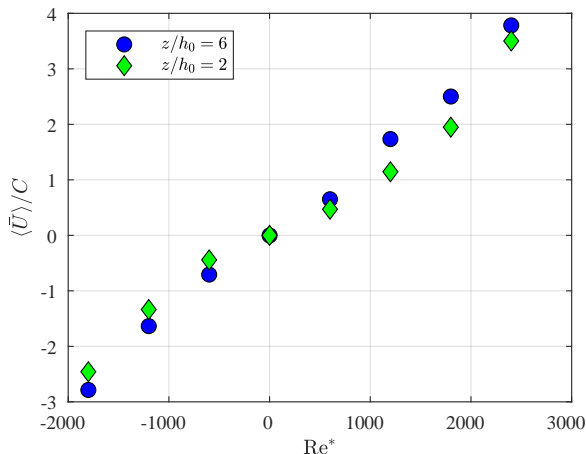


Figure 2. Nondimensional x - and time-averaged wind speed $\langle \bar{U} \rangle / C$ (2.14) versus wind Reynolds number Re^* (2.9) at heights $z/h_0 = 6$ (blue) and $z/h_0 = 2$ (green diamonds).

257 the model-domain x -averaged wind velocity $\bar{U}(z/h_0, \tilde{t})$, defined as,

$$\bar{U}(z/h_0, \tilde{t}) = \frac{1}{L_x/h_0} \int_0^{L_x/h_0} u(x/h_0, z/h_0, \tilde{t}) d(x/h_0) \quad (2.13)$$

258 where $L_x/h_0 = 60$ is the length of the model domain (figure 1). As will be seen, the earliest
 259 solitary wave overturning occurs at $\tilde{t} = 19.13$. Thus, we define the period for time-averaging over
 260 $1 < \tilde{t} < 19$, which represents time-period of solitary wave evolution prior to overturning. During
 261 this time-period, the wind was largely steady. The time- and x -averaged air velocity $\langle \bar{U} \rangle$ is defined
 262 as

$$\langle \bar{U} \rangle(z/h_0) = \frac{1}{18} \int_1^{19} \bar{U}(z/h_0, \tilde{t}) d\tilde{t}, \quad (2.14)$$

263 is only a function of the vertical z/h_0 , and is evaluated only for $z/h_0 \geq 1$ which is always air.
 264 We define the nondimensional wind speed as $\langle \bar{U} \rangle / C$. Statistics of the nondimensional wind are
 265 presented in Appendix B.

266 We compare Re^* and $\langle \bar{U} \rangle / C$ at two vertical locations $z/h_0 = \{2, 6\}$ (figure 2). The first
 267 location $z/h_0 = 2$ is representative of near-surface wind but is still at least two solitary wave
 268 amplitudes a_0/h above the air-water interface. The second $z/h_0 = 6$ represents the height of wind
 269 measurements in the field-scale experiments (Feddersen *et al.* 2023). For $z/h_0 = 6$, $\langle \bar{U} \rangle / C$ is
 270 largely linear with Re^* (figure 2, circles) with $\langle \bar{U} \rangle / C = 3.8$ for $Re^* = 2400$ and $\langle \bar{U} \rangle / C = -2.8$ for
 271 $Re^* = -1800$. The linear relationship indicates that the stress is not due to turbulence and that
 272 Re^* is a proxy for $\langle \bar{U} \rangle / C$. At $z/h_0 = 2$, $\langle \bar{U} \rangle / C$ is slightly weaker than at $z/h_0 = 6$ and has a weak
 273 quadratic trend (green diamonds in figure 2) with $\langle \bar{U} \rangle / C = 3.5$ at $Re^* = 2400$ and $\langle \bar{U} \rangle / C = -2.5$
 274 at $Re^* = -1800$. At both z/h_0 , the model $\langle \bar{U} \rangle / C$ range is larger than in field-scale observations
 275 where significant wind-effects on wave overturns occurred over $-1.2 < U/C < 0.8$. Based on
 276 the $\langle \bar{U} \rangle / C$ and Re^* relationship (figure 2), this corresponds to $|Re^*| < 1200$. Although modeling
 277 results will be analyzed using Re^* , we will keep this relationship in mind.

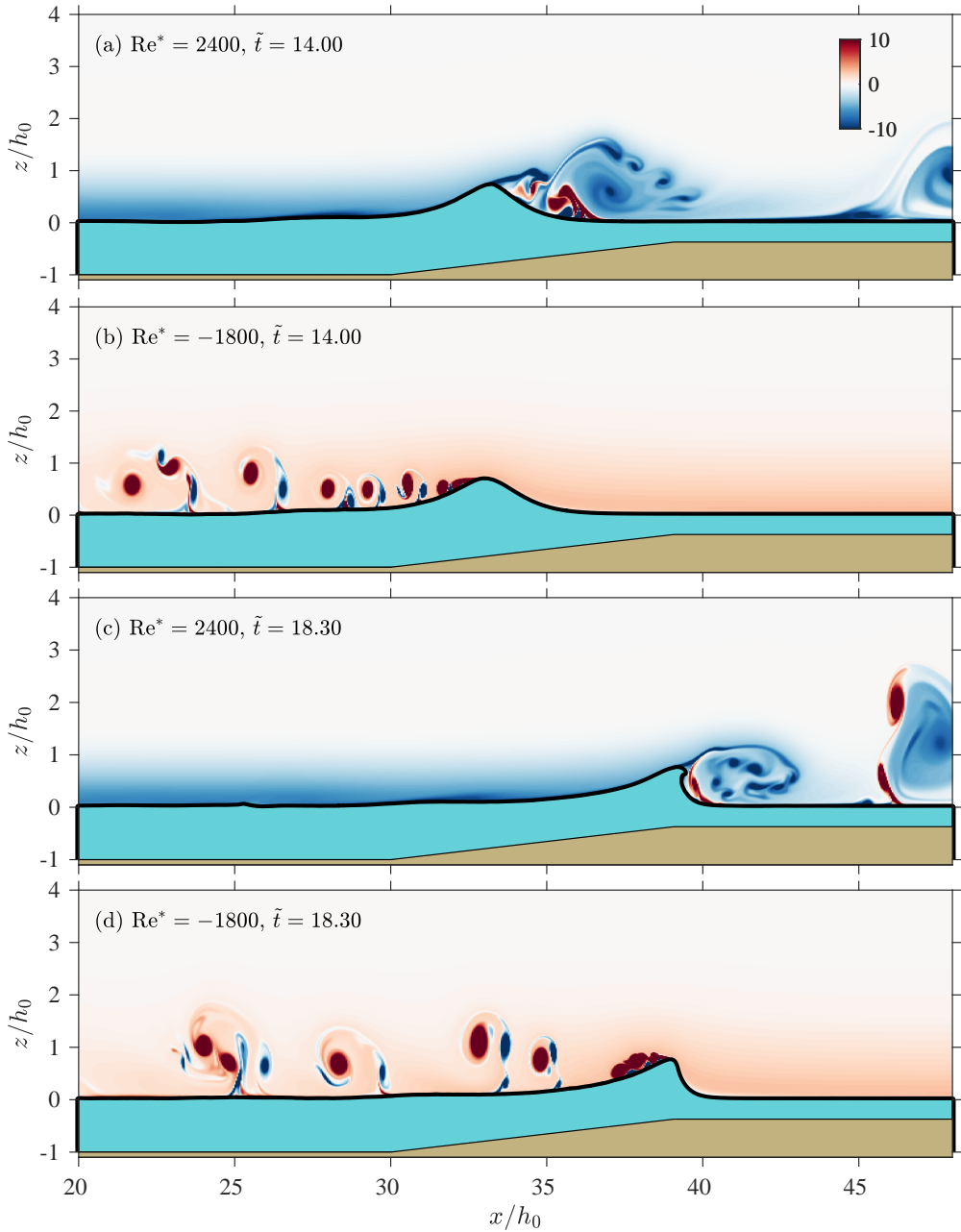


Figure 3. The solitary wave in water (aqua blue) shoaling over the bathymetry (brown) with overlaid air vorticity as a function of horizontal x/h_0 and vertical z/h_0 coordinates for times (a,b) $\tilde{t} = 14$ and (c,d) $\tilde{t} = 18.30$ for (a,c) strong onshore wind $Re^* = 2400$ and (b,d) strong offshore wind $Re^* = -1800$. The air-water interface is indicated by the black curve.

3. Results

3.1. Description of solitary wave transformation under wind

We now present qualitative features of the solitary wave shoaling for the strongest onshore ($\text{Re}^* = 2400$) and offshore ($\text{Re}^* = -1800$) wind (figure 3) at two different times during shoaling. For both Re^* , the modeled solitary wave speed is slightly faster than the small a_0/h_0 analytic $\tilde{C} = 1.265$. Onshore and offshore wind implies wind blowing in the $+x$ and $-x$ directions, respectively. The conventions used are as follows. Front and back of the solitary wave are in relation to the direction of $+x$ solitary wave propagation. Upstream and lee of the solitary wave are in relation to the airflow direction. At $\tilde{t} = 14.0$, the $\text{Re}^* = 2400$ solitary wave has propagated up the slope and has amplified from initial amplitude $a_0/h_0 = 0.6$ to a peak $\eta_{\text{pk}}/h_0 = 0.71$ at $x_{\text{pk}}/h_0 = 33.2$ (figure 3a). Wind is in the direction of solitary wave propagation and is faster than the solitary wave speed with $\langle \bar{U} \rangle / C \approx 3.4$ at $z/h_0 = 2$ (figure 2). The shoaling solitary wave has also changed shape asymmetrically, characteristic of shoaling solitary waves (e.g. Knowles & Yeh 2018; Mostert & Deike 2020; Zdyrski & Feddersen 2022). The asymmetric front-face minimum steepness (slope) $\min(\partial\eta/\partial x) = -0.46$ and the back-face maximum slope $|\partial\eta/\partial x| = 0.32$, both larger than initial solitary wave maximum slope magnitude $|\partial\eta/\partial x| = 0.25$, indicate solitary wave shoaling. Upstream of the solitary wave, the airflow is laminar with the strongest negative vorticity concentrated at the air water interface. In the lee of the solitary wave, the airflow has separated and strong turbulence and turbulent ejections are present near the front face of the wave with positive and negative nondimensional vorticity near 10. At $\tilde{t} = 14.00$, the $\text{Re}^* = -1800$ solitary wave has propagated up the slope with maximum $\eta_{\text{pk}}/h_0 = 0.68$ at $x_{\text{pk}}/h_0 \approx 33.0$ (figure 3b), slightly slower than for the $\text{Re}^* = 2400$ simulation. The wind blows counter the direction of solitary wave propagation and at $z/h_0 = 2$ the nondimensional wind speed is $\langle \bar{U} \rangle / C \approx -2.4$ (figure 2). Upstream, the airflow is laminar with strongest positive vorticity near the air water interface. In the lee of the solitary wave, the airflow separates with a trail of quasi-regular vortices ejected off of the back face of the wave, that are smaller than that for the onshore wind case (figure 3a). The offshore-wind solitary wave has weaker front face minimum slope $\min(\partial\eta/\partial x) = -0.37$ and weaker maximum rear face slope $|\partial\eta/\partial x| = 0.31$, relative to the onshore wind case. These differences in solitary wave slope between $\text{Re}^* = 2400$ and $\text{Re}^* = -1800$ suggest the wind is at $\tilde{t} = 14.0$ already having an effect on the solitary wave.

Later at $\tilde{t} = 18.30$, the differences between the $\text{Re}^* = 2400$ and $\text{Re}^* = -1800$ solitary wave are even starker. At $\tilde{t} = 18.30$, the $\text{Re}^* = 2400$ solitary wave peak is located at $x_{\text{pk}}/h_0 \approx 39.2$ and has transformed substantially (figure 3c). The overturning jet has just formed as the front face slope goes beyond vertical with maximum $\eta/h_0 = 0.74$ and infinite maximum steepness. The back face, with maximum $|\partial\eta/\partial x| = 0.3$, is even more gently sloped than the back-face at $\tilde{t} = 14.0$. The airflow is laminar upstream of the solitary wave, and the airflow separates on the front face of the wave with recirculating vortices. At $\tilde{t} = 18.30$, the $\text{Re}^* = -1800$ solitary wave is quite different from the $\text{Re}^* = 2400$ solitary wave. The solitary wave peak is located at $x_{\text{pk}}/h_0 = 39.0$ with maximum height $\eta_{\text{pk}}/h_0 = 0.74$ and although the front-face has steepened significantly with maximum steepness of $|\partial\eta/\partial x| = 2.15$, the overturning jet has not yet formed (figure 3d). The back-face maximum slope is much weaker at $|\partial\eta/\partial x| = 0.3$. The upstream airflow is laminar, but the airflow separation near the crest is more intense than at $\tilde{t} = 14.0$ as the wave is steeper and lee vortices continue to be shed. The differences in the shoaling solitary wave for onshore and offshore wind both during shoaling ($\tilde{t} = 14.0$) and the stronger differences at- or near-overturning at ($\tilde{t} = 18.30$) demonstrate wind-effects on solitary wave shoaling.

3.2. Statistics of solitary wave shoaling under wind

We next examine statistics of soliton shoaling under wind. As before, η_{pk}/h_0 is the peak of the air-water interface associated with the solitary wave, with horizontal location x_{pk}/h_0 . As the

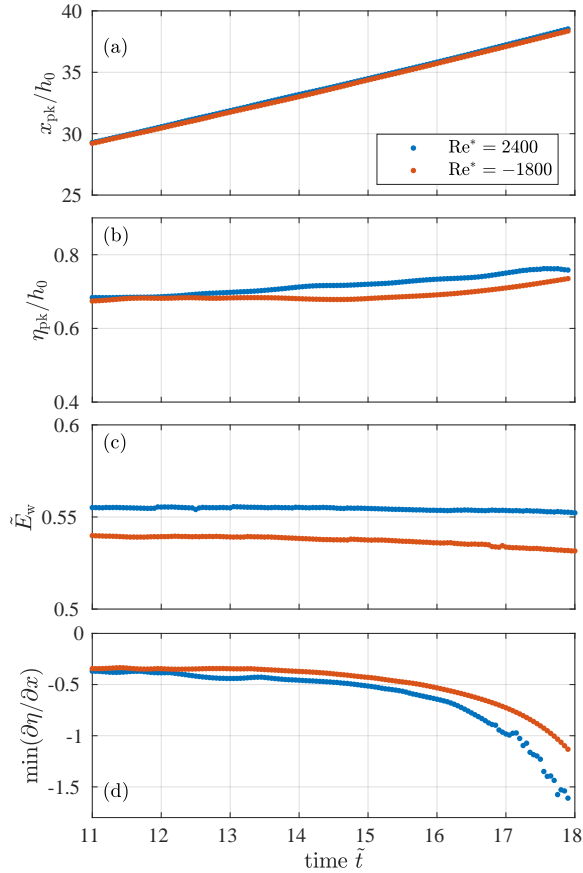


Figure 4. Statistics of solitary wave shoaling under wind versus nondimensional time \tilde{t} for $\text{Re}^* = 2400$ and $\text{Re}^* = -1800$: (a) horizontal location of peak water elevation x_{pk}/h_0 , (b) maximum water elevation η_{pk}/h_0 , (c) nondimensional water energy \tilde{E}_w (2.11) and (d) minimum air-sea interface slope $\min(\partial\eta/\partial x)$. The time period shown $11 < \tilde{t} < 17.9$ corresponds to solitary wave shoaling on the slope until just prior to the slope going vertical for $\text{Re}^* = 2400$.

solitary wave surface is fully refined, both have uncertainty of 3.7×10^{-3} , far smaller than the horizontal and vertical scales of the solitary wave. The minimum slope on the front face of the solitary wave is defined as $\min(\partial\eta/\partial x)$. We also examine the nondimensional water energy \tilde{E}_w (2.12). These parameters are estimated from $\tilde{t} = 11$ to $\tilde{t} = 17.9$ corresponding to the time when shoaling on the slope commences to just prior to when the $\text{Re}^* = 2400$ slope goes vertical.

For all cases x_{pk}/h_0 is largely a linear function of \tilde{t} (figure 4a), indicating largely constant propagation speed as the solitary wave shoals over the rapidly varying bathymetry. The lack of significant solitary wave deceleration is similar to other model simulations over rapidly varying bathymetry (Guyenne & Grilli 2006) and observations at the Surf Ranch (Feddersen *et al.* 2023). For both Re^* , a least-squares fit between time and x_{pk}/h_0 yields skill exceeding $r^2 > 0.99$. For $\text{Re}^* = 2400$, the fit solitary wave speed is $\tilde{C} = 1.33$. For $\text{Re}^* = -1800$, the fit solitary wave speed $\tilde{C} = 1.32$ is slightly slower, indicating that wind has only a small effect on propagation speed. Both fit speeds are slightly larger than the theoretical solitary wave speed of $\tilde{C} = 1.265$. Deviations from the linear fit indicate a weak slowing $\Delta\tilde{C} \approx 0.05$ for $\tilde{t} < 15$ and a similar weak acceleration for

$\tilde{t} > 15$, consistent with previous modeling of shoaling solitary waves (Grilli *et al.* 1994). Prior to shoaling, the GN-based solitary wave initial condition with $a_0/h = 0.6$ has adjusted to a narrower and slightly taller shape while also shedding minor trailing transients. During adjustment, water energy is conserved indicating it is not wind driven. The result is a larger value solitary wave height ($\eta_{pk}/h_0 \approx 0.68$) for both Re^* (figure 4b), as shoaling starts, qualitatively consistent with the fit \tilde{C} being larger than expected from theory. This adjustment to the initial condition is consistent for all Re^* . As the solitary wave shoals up the steep slope, η_{pk}/h_0 slowly grows and even close to overturning, η_{pk}/h_0 is still < 0.77 . Overall, the solitary wave amplitude shoaling (η_{pk}/a_0) is slightly slower than Green's law $(h/h_0)^{-1/4}$, similar to BEM simulations on a similar slope (Grilli *et al.* 1994), and consistent with the large-slope and significant nonlinearity regime of Knowles & Yeh (2018). The $Re^* = 2400$ solitary wave does have larger η_{pk}/h_0 during much of shoaling but as the solitary wave steepens significantly near $\tilde{t} = 17.9$, the η_{pk}/h_0 reduces slightly as overturning nears. Similar features can be seen in the simulations of Grilli *et al.* (1997).

The wave energy \tilde{E}_w changes marginally during shoaling ($11 < \tilde{t} < 17.9$) between $Re^* = 2400$ and $Re^* = -1800$ (figure 4c). At $\tilde{t} = 11$, \tilde{E}_w is slightly (two percent) larger ($\tilde{E}_w = 0.554$) for $Re^* = 2400$ relative to $Re^* = -1800$ ($\tilde{E}_w = 0.542$). For $Re^* = -1800$, \tilde{E}_w decays weakly to $\tilde{E}_w = 0.532$ at $\tilde{t} = 17.9$, reflecting both the offshore wind slowly extracting energy from the solitary wave and small viscous dissipation at the wave Reynolds number $Re_w = 4 \times 10^4$. For $Re^* = 2400$, the wave energy \tilde{E}_w is essentially constant during shoaling with $\tilde{E}_w = 0.553$ at $\tilde{t} = 17.9$, as small onshore wind energy input and weak viscous dissipation largely balance. Over this short duration of shoaling, for these extremal Re^* , energy transfer between wind and the solitary wave is weak, which is even more true for the other Re^* .

Unlike η_{pk}/h_0 and \tilde{E}_w , the minimum slope $\min(\partial\eta/\partial x)$ evolves significantly during shoaling with strong differences between $Re^* = 2400$ and $Re^* = -1800$ (figure 4d). At $\tilde{t} = 11$, $\min(\partial\eta/\partial x) \approx -0.36$ for both Re^* with slightly more negative $\min(\partial\eta/\partial x)$ for $Re^* = 2400$. As discussed in Section 3.1, by $\tilde{t} = 14$, the differences in $\min(\partial\eta/\partial x)$ between the two Re^* have grown substantially with $\min(\partial\eta/\partial x) = -0.46$ for $Re^* = 2400$ and $\min(\partial\eta/\partial x) = -0.37$ for $Re^* = -1800$. For both Re^* , $\min(\partial\eta/\partial x)$ continues to evolve rapidly with large differences between Re^* for $\tilde{t} > 15$. For example, by $\tilde{t} = 17.0$ the $Re^* = 2400$ $\min(\partial\eta/\partial x) = -0.98$ whereas the $Re^* = -1800$ $\min(\partial\eta/\partial x) = -0.73$ is smaller in magnitude. Shortly thereafter at $\tilde{t} = 17.9$, $\min(\partial\eta/\partial x) = -1.61$ and -1.13 for $Re^* = 2400$ and 1800 , respectively, indicating the rapid evolution. These strong differences in $\min(\partial\eta/\partial x)$ for the two Re^* indicate wind effects during shoaling.

3.3. The moment of overturning jet impact

We examine the moment in time when the overturning jet impacts the water surface in front of it for three different wind speeds (figure 5). We note that the plunging jet is almost entirely resolved at the smallest AMR nondimensional mesh size (3.7×10^{-3}), and thus the plunging jet, with non-dimensional cross-jet width ≈ 0.05 is well resolved. The time of impact is defined as the earliest time at which the vertical separation between the lowest part of the overturning jet and the water surface below it is $\Delta z/h_0 \leq 0.015$, or 2.5% of the initial solitary wave amplitude $a_0/h_0 = 0.6$. This is also about $4\times$ the minimum model nondimensional resolution of 3.7×10^{-3} . With this time of impact definition, the jet is just about to impact but has not quite yet. The breakpoint location x_{bp}/h_0 is defined as the horizontal location of smallest $\Delta z/h_0$. At the time resolution of model output $\Delta\tilde{t} = 0.01$, occasionally the impact time is chosen when the jet has just made contact with the surface below, and then x_{bp}/h_0 is defined as the smallest location to cross $z/h_0 = 0$. This breakpoint location definition is analogous to that used in Feddersen *et al.* (2023).

For $Re^* = 2400$, the moment of jet impact occurs at $\tilde{t} = 19.13$ making contact at $x_{bp}/h_0 = 40.85$ (figure 5a). The overturn has the classical parametric cubic shape (Longuet-Higgins 1982) seen in both models and observations of wave overturning. The $Re^* = 2400$ overturning jet is relatively thin and the overturn orientation is relatively inclined. For $Re^* = 0$, overturning-jet impact occurs

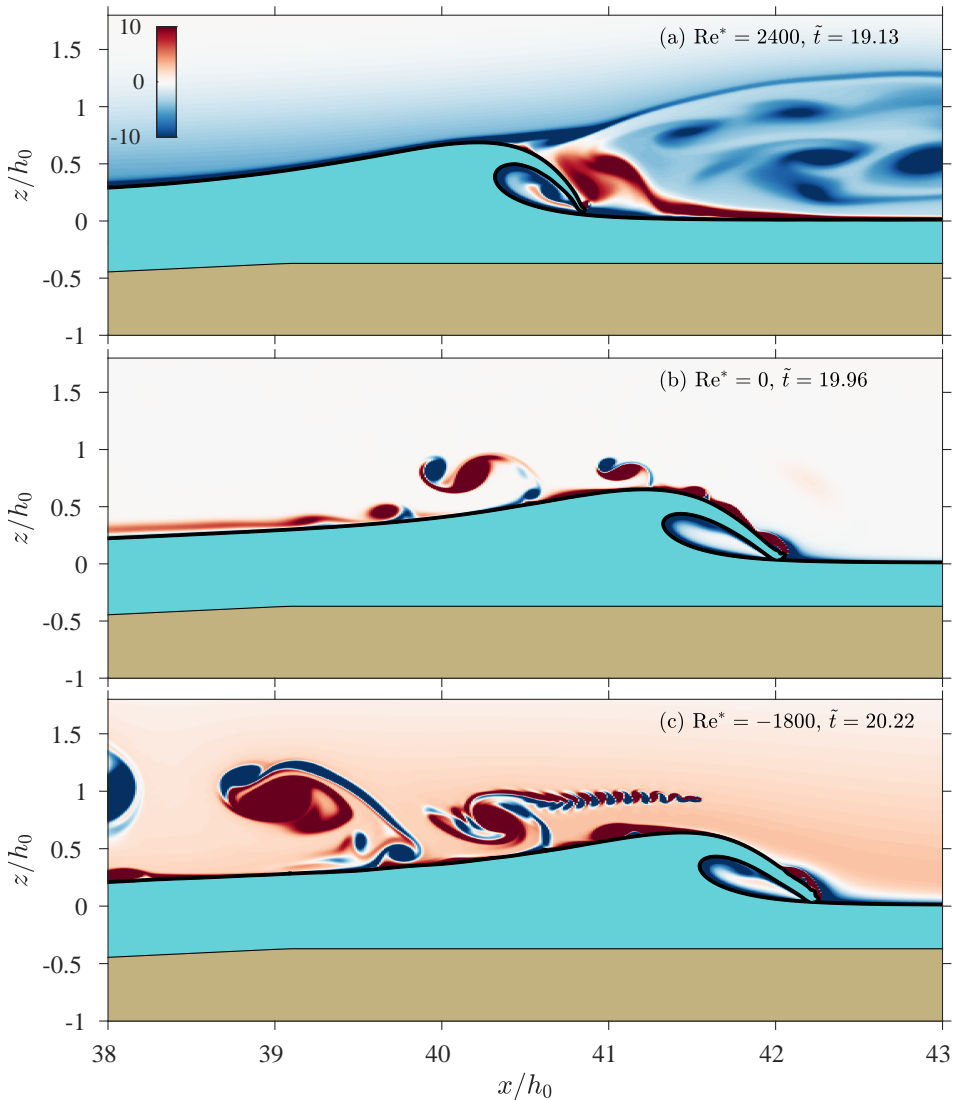


Figure 5. Overturning solitary wave (aqua blue) at the moment of overturning jet impact on the water surface, with the bathymetry (brown) and overlaid air vorticity as a function of horizontal x/h_0 and vertical z/h_0 coordinates: (a) Onshore wind $\text{Re}^* = 2400$ and $\tilde{t} = 19.13$, (b) no wind, $\text{Re}^* = 0$ and $\tilde{t} = 19.96$, and (c) offshore wind $\text{Re}^* = -1800$ and $\tilde{t} = 20.22$. The air-water interface is indicated by the black curve.

389 at $\tilde{t} = 19.96$ at $x_{\text{bp}}/h_0 = 42.05$ (figure 5b), farther onshore and later than for $\text{Re}^* = 2400$. Relative
 390 to $\text{Re}^* = 2400$, the $\text{Re}^* = 0$ maximum height of the wave is slightly reduced, the overturning jet is
 391 thicker, and the overturn is longer and oriented more horizontal. Although, in the fixed reference
 392 frame, the air velocity is essentially zero at $z/h_0 \geq 2$ (figure 2), as the solitary wave moves with
 393 speed near \bar{C} , the relative air velocity is substantial, and vortices are shed behind the overturning
 394 solitary wave. For $\text{Re}^* = -1800$, the overturning jet impact occurs even later at $\tilde{t} = 20.22$ and is
 395 located at $x_{\text{bp}}/h_0 = 42.25$ (figure 5c). Relative to $\text{Re}^* = 0$, the $\text{Re}^* = -1800$ has an even thicker
 396 overturn jet and a longer overturn, which is oriented even more horizontally. The farther offshore
 397 overturning jet-impact with onshore wind ($\text{Re}^* = 2400$) relative to offshore wind ($\text{Re}^* = -1800$)

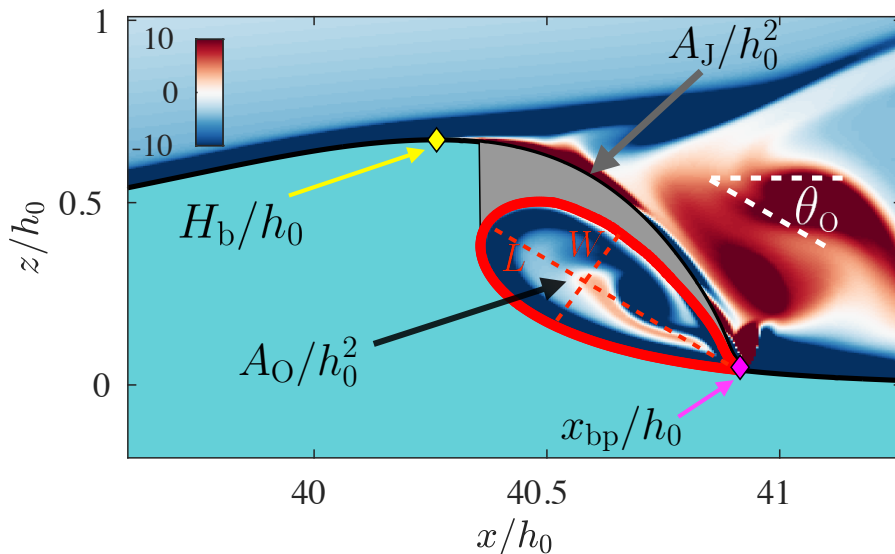


Figure 6. Overturning solitary wave (aqua blue) at the moment of overturning jet impact on the water surface with overlaid air vorticity as a function of horizontal x/h_0 and vertical z/h_0 coordinates for the $Re^* = 2400$ case and definitions for the geometrical properties of the overturning wave. The air-water interface is represented by the black curve. The magenta diamond indicates the nondimensional breakpoint location x_{bp}/h_0 and the yellow diamond indicates the nondimensional breaking wave height H_b/h_0 . The red curve indicates the enclosed overturn region with area A_o/h_0^2 , and the gray region indicates the overturning jet area A_J/h_0^2 . The dashed red lines schematize the length L and width W of the overturn. The overturn orientation relative to horizontal θ_o is indicated.

398 is consistent with laboratory (Douglass 1990) and field scale experiments (Feddersen *et al.* 2023)
 399 experiments.

400 We note in passing that a vortex street is visible in the lee of the overturning wave in figure 5c.
 401 This is the wake of a small droplet torn from the crest of the wave during the initial stage of
 402 overturning. Such droplets occasionally appear in the simulations we present, but they are rare,
 403 have negligible mass and momentum, and therefore do not affect the dynamics of the evolving
 404 breaker. Such droplets do not have great physical significance in this 2D setting. For field-scale
 405 overturning waves, which DNS models cannot yet capture in 3D, plentiful spray droplets appear
 406 during the overturn but their effects on the geometry and dynamics of the overturning breaker are
 407 as yet unknown.

3.4. Definition of Geometrical Parameters of Wave Overturning

408
 409 Here, we define geometrical parameters of the overturning wave at the moment of jet-impact for
 410 the $Re^* = 2400$ case (figure 6) following the methodology used in the experimental study over wave
 411 overturning (Feddersen *et al.* 2023). We note that the shape of the overturning wave (Figure 6)
 412 including the jet are similar to those seen in fully nonlinear potential flow simulations (Grilli
 413 *et al.* 1997) and in laboratory experiments of overturning solitary waves (Li & Raichlen 2003)
 414 indicating that wave overturning is well resolved. The first geometrical parameter is the breakpoint
 415 location x_{bp}/h_0 (magenta diamond in figure 6). The breaking wave height H_b/h_0 is defined as
 416 the maximum elevation of the air-water interface (yellow diamond in figure 6), as no trough is present
 417 in front of the solitary wave, i.e., $z/h_0 = 0$ (figure 3, 5). The overturn boundary enclosing the air
 418 within the overturn (red curve in figure 6) has area A_o/h_0^2 (figure 6). The region of the overturning
 419 jet is defined as the upper region of water where the air-water interface is multi-valued in x/h_0 ,

with area A_J/h_0^2 (gray region in figure 6). Note, overturning jet area was not measured in previous studies. As done previously for overturn area (O’Dea *et al.* 2021; Feddersen *et al.* 2023), both overturn area and jet area are normalized by H_b/h_0 so that analysis is performed on A_o/H_b^2 and A_J/H_b^2 . The overturn boundary has shape similar to the functional form (Longuet-Higgins 1982) used previously to fit laboratory and field measured wave overturns (e.g. Blenkinsopp & Chaplin 2008; O’Dea *et al.* 2021; Feddersen *et al.* 2023). Overturn length L and width W (figure 6) are estimated by rotating the overturn boundary by the overturn angle θ_o (figure 5) to the horizontal and fitting to the functional form (Longuet-Higgins 1982)

$$\frac{z'}{W} = \pm \frac{3\sqrt{3}}{4} \sqrt{\frac{x'}{L}} \left(\frac{x'}{L} - 1 \right), \quad (3.1)$$

where the x' and z' coordinates are oriented along and across the overturn, and L and W are the overturn length and width (figure 7). Consistent with results from laboratory and field (Blenkinsopp & Chaplin 2008; O’Dea *et al.* 2021; Feddersen *et al.* 2023), the modeled overturn boundary is well fit to the functional form (3.1) for all Re^* .

3.5. Geometrical Parameters dependence on Wind

Across all Re^* , x_{bp}/h_0 varies from 40.9 to 42.2 with smaller x_{bp}/h_0 (farther offshore) for increasing Re^* as in figure 5. To highlight wind effects, we define a demeaned breakpoint location as

$$\frac{\Delta x_{bp}}{h_0} = \frac{\langle x_{bp} \rangle}{h_0} - \frac{x_{bp}}{h_0}, \quad (3.2)$$

where $\langle \rangle$ is an average over the eight simulations at different Re^* . Thus, positive $\Delta x_{bp}/h_0$ is farther offshore, consistent with previous experiment work (Douglass 1990; Feddersen *et al.* 2023). From no-wind ($Re^* = 0$) to onshore wind (positive Re^*), $\Delta x_{bp}/h_0$ increases rapidly from -0.2 to 0.9, with the largest increase at larger Re^* (figure 7a). From no-wind to offshore wind (negative Re^*), $\Delta x_{bp}/h_0$ decreases more slowly with Re^* than for onshore wind reaching $\Delta x_{bp}/h_0 = -0.4$ at $Re^* = -1800$ (figure 7a). This breakpoint dependence on the wind is qualitatively consistent with experimental results (Douglass 1990; Feddersen *et al.* 2023). Normalizing the field-scale results of Feddersen *et al.* (2023) by h_0 as we do here, yields observed field-scale $\Delta x_{bp}/h_0$ variation of ± 0.8 consistent with modeled $\Delta x_{bp}/h_0$ variation. However, the field-scale variation occurs from substantially weaker wind variations than seen in the modeling, as will be discussed. We next examine the effect of wind on the breaking wave height H_b/h_0 . For no wind ($Re^* = 0$), $H_b/h_0 = 0.64$ and for onshore wind H_b/h_0 increases to $H_b/h_0 = 0.674$ for $Re^* = 2400$ (figure 7b). From no wind to offshore wind, the H_b/h_0 decreases slightly to $H_b/h_0 = 0.627$. Note that this range of H_b/h_0 is a reduction relative to the largest values of η_{pk}/h_0 during shoaling (figure 4b), similar to potential flow simulations of overturning solitary waves (Grilli *et al.* 1997).

We now examine wind effects on nondimensional overturn area A_o/H_b^2 (figure 7c). From no-wind ($Re^* = 0$) to onshore wind, A_o/H_b^2 decreases from $A_o/H_b^2 = 0.352$ at $Re^* = 0$ to $A_o/H_b^2 = 0.301$ at $Re^* = 2400$. From no-wind to offshore wind, A_o/H_b^2 is relatively constant before decreasing slightly to $A_o/H_b^2 = 0.344$ at $Re^* = -1800$. This relationship with A_o/H_b^2 and Re^* is qualitatively consistent with field-scale experiment (Feddersen *et al.* 2023). However, the experimental A_o/H_b^2 varied between 0.2 and 0.4, a larger variation than seen in the model, for weaker wind or Re^* variation. Next, we examine the overturn aspect ratio W/L (figure 7d). For no-wind, $W/L = 0.300$ and increases for onshore wind to $W/L = 0.381$ at $Re^* = 2400$. For offshore wind, W/L is largely constant varying from 0.296 to 0.305. This pattern of increasing W/L with positive Re^* is inconsistent with the experimental results of Feddersen *et al.* (2023), who found W/L decreased with increasing onshore wind. Furthermore, the experimental results had larger W/L range, varying from 0.3 to 0.5, larger than the 0.3 to 0.38 modeled variation in W/L .

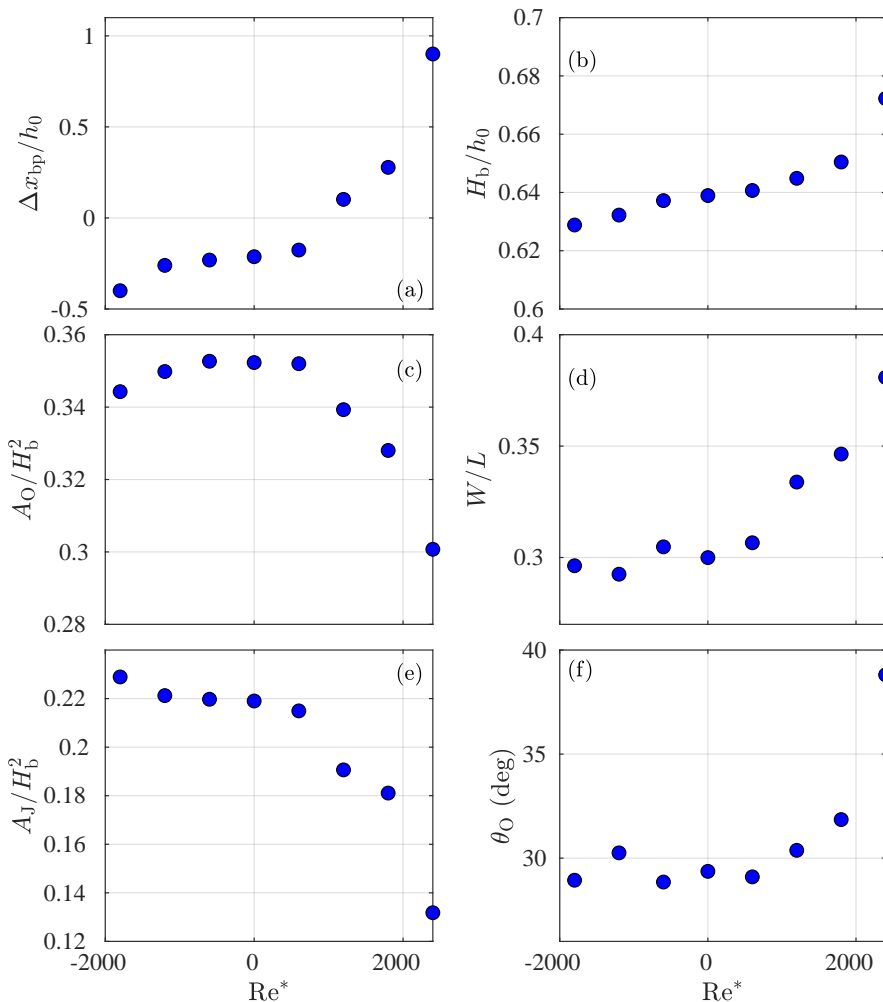


Figure 7. Geometrical parameters of the overturning wave as a function of wind Reynolds number Re^* : (a) Demeaned nondimensional breakpoint location $\Delta x_{bp}/h_0$ (3.2) (b) wave height at breaking H_b/h_0 , (c) nondimensional wave overturn area A_o/H_b^2 , (d) overturn aspect ratio W/L , and (e) nondimensional wave jet area A_J/H_b^2 , (f) overturn angle θ_o .

463 We next examine the wind effect on the non-dimensional jet area A_J/H_b^2 (figure 7e). For no-wind,
 464 $A_J/H_b^2 = 0.219$, which decreases rapidly with onshore wind to $A_J/H_b^2 = 0.132$ for $Re^* = 2400$.
 465 For offshore wind, A_J/H_b^2 is largely constant with Re^* , varying from 0.229 to 0.219. Overturn
 466 jet area has not been previously examined experimentally or numerically. Lastly, we examine the
 467 overturn angle θ_o (figure 7f). For $Re^* = 0$, the overturn angle $\theta_o = 29^\circ$ and this increases with
 468 onshore wind to $\theta_o = 39^\circ$ for $Re^* = 2400$, consistent with the orientations of the overturn seen
 469 in figure 5a,b. For offshore wind, θ_o varies only weakly with negative Re^* . This range of θ_o is
 470 smaller than the $\theta_o \approx 42^\circ \pm 8^\circ$ at the Surf Ranch (Feddersen *et al.* 2023). It is also on the low end
 471 of $30^\circ < \theta_o < 60^\circ$ reported in surfzone overturning waves (O’Dea *et al.* 2021).

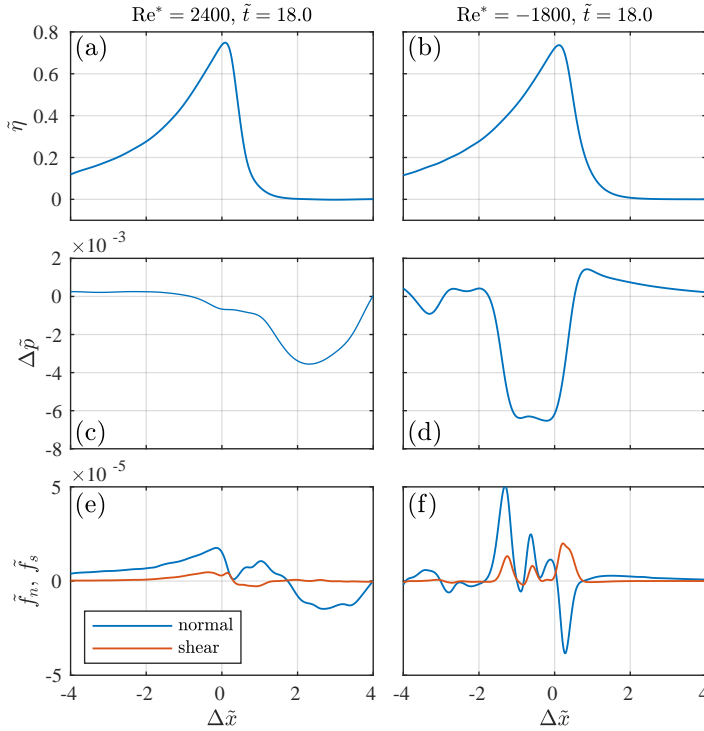


Figure 8. Snapshots at $\tilde{t} = 18.0$ of (top) $\tilde{\eta}$, (middle) $\Delta\tilde{p}$, and (bottom) viscous normal \tilde{f}_n and shear \tilde{f}_s stresses versus $\Delta\tilde{x}$ for (left) $\text{Re}^* = 2400$ and (right) $\text{Re}^* = -1800$.

3.6. Relative strength of pressure and shear stress

472

473 Airflow can affect the water-based solitary wave via two mechanisms on the air-water interface.
 474 The first mechanism is through an air-flow induced pressure, and the second mechanism either
 475 normal or shear viscous stresses. Here we will examine the relative strength of pressure and
 476 viscous stresses on the air-water interface at a shoaling time just prior to when η goes multivalued.
 477 Henceforth, we will use nondimensional variables indicated with a $\tilde{}$. As discussed in Section 2.1.6,
 478 air pressure and velocity gradients are output and estimated at a small nondimensional distance
 479 $\Delta = 0.01$ normal to the air-water interface. This prevents biases in pressure estimation due to noise
 480 in air-water interface curvature estimates. From the velocity gradients, the nondimensional viscous
 481 stress tensor $\tilde{\mathbf{S}}$ is (in index notation)

$$\tilde{S}_{ij} = \tilde{\mu}_a \left(\frac{\partial \tilde{u}_i}{\partial \tilde{x}_j} + \frac{\partial \tilde{u}_j}{\partial \tilde{x}_i} \right) \quad (3.3)$$

482 where the nondimensional air dynamic viscosity is $\tilde{\mu}_a = \text{Re}_w^{-1} \mu_a / \mu_w = 4.53 \times 10^{-7}$. The normal
 483 ($\tilde{\mathbf{n}}$) and parallel ($\tilde{\mathbf{s}}$) unit vectors to the air-water interface are also estimated. At the air-water
 484 interface η , the viscous normal stress is $\tilde{f}_n = \tilde{\mathbf{n}} \cdot \tilde{\mathbf{S}} \cdot \tilde{\mathbf{n}}$ and the viscous shear stress is $\tilde{f}_s = \tilde{\mathbf{s}} \cdot \tilde{\mathbf{S}} \cdot \tilde{\mathbf{n}}$.
 485 To isolate the pressure disturbance associated with the solitary wave, the air-water interface
 486 nondimensional pressure differential $\Delta\tilde{p}$ is estimated as the pressure \tilde{p} minus an upstream pressure
 487 located at $\Delta\tilde{x} = \pm 6$ depending on the wind direction.

488 We examine the end of the shoaling period at $\tilde{t} = 18.0$, where the $\text{Re}^* = 2400$ air-water interface
 489 $\tilde{\eta}$ is close to being multivalued. For both $\text{Re}^* = 2400$ and $\text{Re}^* = -1800$ the $\tilde{\eta}(\Delta\tilde{x})$ profile have
 490 classic sawtooth shapes with steep front face and a milder-sloped back face (figure 8a,b), with

491 steeper front face for $\text{Re}^* = 2400$ (e.g. figure 4d). For $\text{Re}^* = 2400$, the windward side of the solitary
 492 wave ($-3 < \Delta\tilde{x} < -1$) has mildly elevated $\tilde{p} \approx 0.2 \times 10^{-3}$ (figure 8c) and on the leeward side (in
 493 front of the wave) a deep low pressure with minimum $\tilde{p} = -3.7 \times 10^{-3}$ occurs over $0 < \Delta\tilde{x} < 4$.
 494 This low pressure is associated with the strongly separated flow that occurs many $\Delta\tilde{x}$ in front of
 495 the wave (figure 3a,b). In contrast, the $\text{Re}^* = -1800$ simulation has much higher $\tilde{p} \approx 1.5 \times 10^{-3}$
 496 on the windward wave face and a deeper low pressure with minimum $\tilde{p} = -6.3 \times 10^{-3}$ in the lee
 497 of the wave (figure 8d). For $\text{Re}^* = -1800$, the lee low-pressure width ($\approx 2\Delta\tilde{x}$ wide) is half as
 498 wide as that for $\text{Re}^* = 2400$ due to the differences flow separation and attachment. On the air-sea
 499 interface, the magnitude of the viscous stresses relative to pressure are generally small (figure 8e,f).
 500 For $\text{Re}^* = 2400$ and $\text{Re}^* = -1800$, both normal and shear stresses have magnitude $< 5 \times 10^{-5}$,
 501 roughly a factor of $100\times$ smaller than that of \tilde{p} . The normal stresses are a factor of $2\text{-}3\times$ larger
 502 than the shear stresses for both $\text{Re}^* = 2400$ and $\text{Re}^* = -1800$. The $\text{Re}^* = -1800$ viscous stresses
 503 are larger than those of $\text{Re}^* = 2400$ due to the stronger shear between the wind blowing counter to
 504 the $+\Delta\tilde{x}$ directed solitary wave velocities.

505 This demonstrates that the pressure forces must be those that are influencing changes in wave
 506 shoaling and overturning. This result at $\tilde{t} = 18.0$ is consistent at other wave shoaling times
 507 $11 < \tilde{t} < 18$ where pressure variability exceeds viscous stresses by $100\times$. These results are
 508 consistent with DNS simulations of wind-wave growth which found pressure about $10\times$ larger
 509 than viscous stresses (Wu *et al.* 2022). They also found that pressure forces grew with wave slope
 510 particularly for smaller wave age, but that viscous forces did not grow. During shoaling, the soliton
 511 is steeper (4d) than any regime of Wu *et al.* (2022). Moreover, Wu *et al.* (2022) investigated a
 512 lower Re^* , for which viscous forces are likely to be stronger relative to inertial effects than for the
 513 strongest Re^* presented here. These observations may explain why our ratio of pressure to viscous
 514 forces is so strong relative to Wu *et al.* (2022).

515 3.7. The Surface Dynamic Boundary Condition

516 With the viscous stresses negligible, we next examine the role of \tilde{p} on the air-water interface $\tilde{\eta}$
 517 using the irrotational flow surface dynamic boundary condition boosted into a moving horizontal
 518 reference frame $\Delta\tilde{x}$ with constant best-fit speed \tilde{C} (figure 4a) for the $\text{Re}^* = 2400$ and $\text{Re}^* = -1800$
 519 cases. In the $\Delta\tilde{x}$ reference frame moving with constant speed \tilde{C} , the nondimensional dynamic
 520 boundary condition is transformed to

$$521 \frac{\partial\tilde{\phi}}{\partial\tilde{t}} - \tilde{C}\tilde{u} + \frac{1}{2} [\tilde{u}^2 + \tilde{w}^2] + \tilde{\eta} + \Delta\tilde{p} = \tilde{T} \quad (3.4)$$

522 where $\tilde{\phi}$ is the nondimensional velocity potential, all terms are evaluated at $\tilde{z} = \tilde{\eta}$, $\Delta\tilde{p}$ is the
 523 pressure jump at the surface, and \tilde{T} represents the nondimensional surface tension term, for which
 the curvature κ from (2.1) can be written in terms of the (single-valued) interface $\tilde{\eta}$

$$524 \tilde{T} = \text{Bo}^{-1} \frac{\partial^2\tilde{\eta}/\partial(\Delta\tilde{x})^2}{(1 + (\partial\tilde{\eta}/\partial(\Delta\tilde{x}))^2)^{3/2}}. \quad (3.5)$$

525 The change in the solitary wave in the moving reference frame is represented by $\partial\tilde{\phi}/\partial\tilde{t}$, and for an
 526 unchanging solitary wave propagating at \tilde{C} , $\partial\tilde{\phi}/\partial\tilde{t} = 0$. Thus, for $\Delta\tilde{p} = 0$ and no surface tension,
 the residual

$$527 \tilde{R} = -\tilde{C}\tilde{u} + \frac{1}{2} [\tilde{u}^2 + \tilde{w}^2] + \tilde{\eta} \quad (3.6)$$

528 is zero for an unchanging solitary wave. Nonzero \tilde{R} can therefore be interpreted as the signature of
 529 the wave's unsteady evolution i.e. of its evolving asymmetry and nonlinear steepening. The terms
 $-\tilde{C}\tilde{u}$, $(1/2)[\tilde{u}^2 + \tilde{w}^2]$, and \tilde{T} also are evaluated on the air-water interface. The terms of (3.4) are

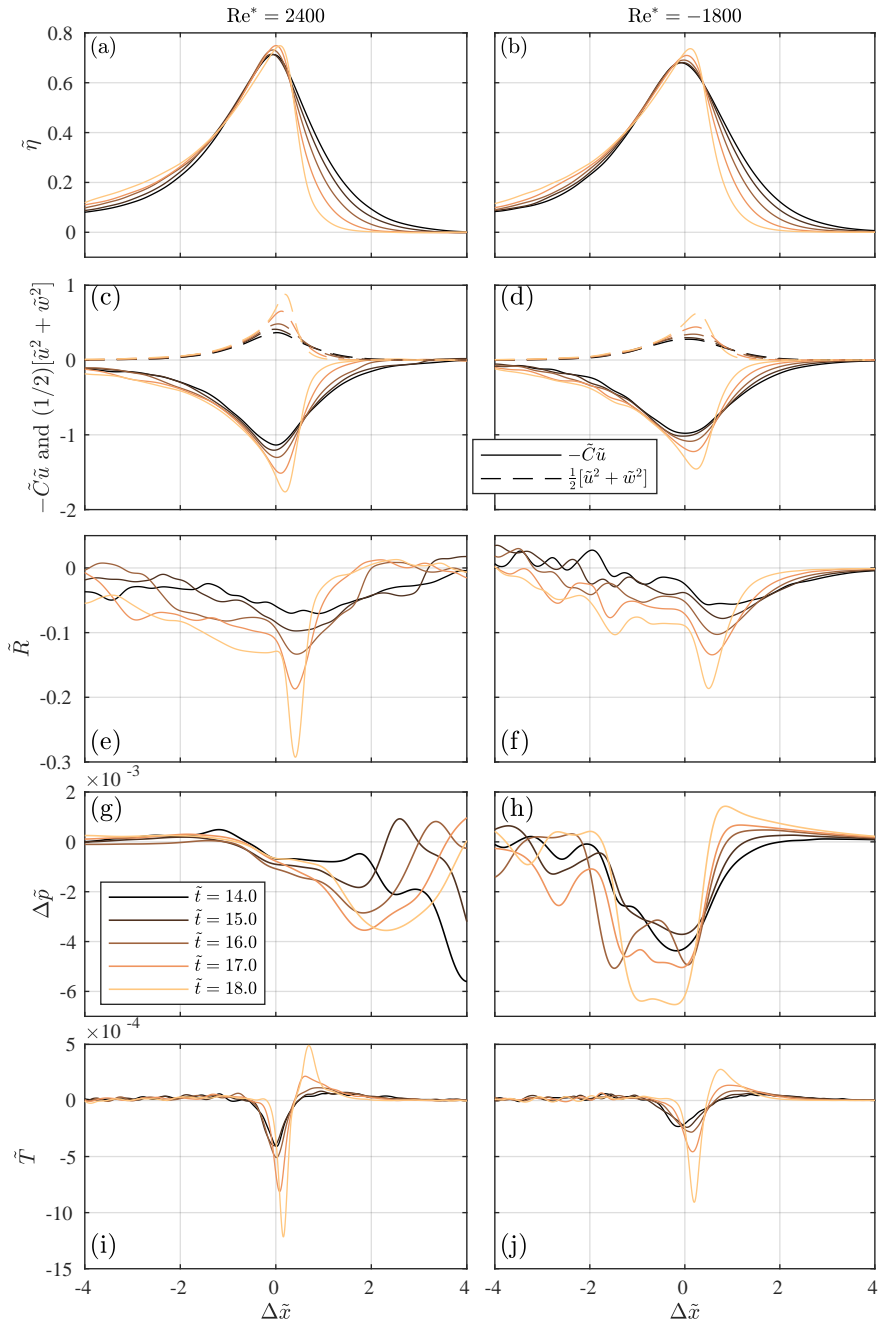


Figure 9. Surface dynamic boundary condition terms (3.4) versus $\Delta\tilde{x}$ for (left) $\text{Re}^* = 2400$ and (right) $\text{Re}^* = -1800$ and from time $\tilde{t} = 14.0$ (black) to $\tilde{t} = 18.0$ (gold) at $\Delta\tilde{t} = 1$: (a,b) $\tilde{\eta}$, (c,d) $-\tilde{C}\tilde{u}$ (solid) and $(1/2)[\tilde{u}^2 + \tilde{w}^2]$ (dashed), (e,f) the residual term \tilde{R} (3.6), (g,h) $\Delta\tilde{p}$, and (i,j) the surface tension term \tilde{T} (3.5).

analyzed during the latter part of the shoaling phase ($14 \leq \tilde{t} \leq 18$) when significant differences in the minimum slope on the front of the wave face occur (figure 4d) and when $\tilde{\eta}$ is still single-valued.

During shoaling ($\tilde{t} = 14.0$ to $\tilde{t} = 18.0$), both $\text{Re}^* = 2400$ and $\text{Re}^* = -1800$ solitary waves evolve from a more symmetrical wave to an asymmetrical sawtooth type pattern (figure 9a,b) as maximum $\tilde{\eta} \approx 0.7$ throughout (as in figure 4a). Although subtle differences between the $\text{Re}^* = 2400$ and $\text{Re}^* = -1800$ solitary waves are evident at $\tilde{t} = 14.0$, by $\tilde{t} = 18.0$, the $\text{Re}^* = 2400$ solitary wave front face is clearly significantly steeper than for $\text{Re}^* = -1800$, consistent with figure 4d. For both Re^* , the peak $-\tilde{C}\tilde{u} \approx -1$ at $\tilde{t} = 14.0$ which grows in time and becomes more asymmetric (solid, figure 9c,d), with $\text{Re}^* = 2400$ having more growth and asymmetry at $\tilde{t} = 18.0$. For both Re^* at $\tilde{t} = 14.0$, the nonlinear term $(1/2)[\tilde{u}^2 + \tilde{w}^2]$ is largely symmetric with maximum of 0.36 and 0.27 for $\text{Re}^* = 2400$ and $\text{Re}^* = -1800$, respectively (dashed, figure 9c,d), indicating wind-induced difference in shoaling at this time. This also indicates that the weakly nonlinear assumption is starting to be questionable, consistent with results from fully versus weakly nonlinear Boussinesq wave models (e.g. Wei *et al.* 1995). With increasing time, $(1/2)[\tilde{u}^2 + \tilde{w}^2]$ increases dramatically to values of 0.88 and 0.63 at $\tilde{t} = 18.0$ and also becomes asymmetric, indicating strong nonlinearity at this time, particularly for $\text{Re}^* = 2400$.

Although the $\tilde{\eta}$, $-\tilde{C}\tilde{u}$, and $(1/2)[\tilde{u}^2 + \tilde{w}^2]$ terms are $O(1)$ (figure 9a-d), the residual term \tilde{R} , that sums these terms, is an order of magnitude smaller (figure 9g,h). At $\tilde{t} = 14.0$, \tilde{R} has a minimum of ≈ -0.06 that is slightly more negative and broader for $\text{Re}^* = 2400$. Although over time \tilde{R} grows broadly in $\Delta\tilde{x}$, for $\tilde{t} \geq 16.0$, \tilde{R} growth is concentrated at the solitary wave's front face ($0 \leq \Delta\tilde{x} \leq 0.7$), which attains minimum value of -0.26 and -0.18 for $\text{Re}^* = 2400$ and $\text{Re}^* = -1800$, respectively. This focussed large \tilde{R} leads to rapid $\tilde{\phi}$ changes leading to overturning.

We have already seen the magnitude of pressure term at $\tilde{t} = 18.0$ is $\Delta\tilde{p} \approx 5 \times 10^{-3}$ (figure 8c,d). Over time from $14.0 \leq \tilde{t} \leq 18.0$, the $\text{Re}^* = 2400$ $\Delta\tilde{p}$ is negative in the lee of the solitary wave ($0 < \Delta\tilde{x} < 2$) and grows with time (figure 9g). In the lee-region but away from the concentrated \tilde{R} ($1 < \Delta\tilde{x} < 2$), $\Delta\tilde{p}$ can be 10% or more of \tilde{R} with the same sign, thus enhancing \tilde{R} . From $14.0 \leq \tilde{t} \leq 18.0$, the $\text{Re}^* = -1800$ $\Delta\tilde{p}$ is also negative in the solitary wave lee ($-1.5 \leq \Delta\tilde{x} \leq 0$) and grows with time. In this region $\Delta\tilde{p}$ can also be 10% of \tilde{R} , but on the rear-face of the soliton. Closer to the time of overturning in the narrow region from $0 \leq \Delta\tilde{x} \leq 0.7$ where \tilde{R} is concentrated, $\Delta\tilde{p}$ is small (1–2%) relative to \tilde{R} . However, the significant $\Delta\tilde{p}$ ($\approx 10\%$ of \tilde{R}) in the lee outside of the concentrated region will, during shoaling, induce slowly growing wind-induced differences in wave shape that manifest themselves forward in time until the overturning jet impacts.

As our $\text{Bo} = 4000$ is not at field scale, we also examine the surface tension term \tilde{T} (figure 9i,j). For $\tilde{t} \leq 16.0$, the \tilde{T} term is concentrated near $\Delta\tilde{x} = 0$ and is an order of magnitude smaller than $\Delta\tilde{p}$. However, \tilde{T} grows rapidly at the later stages of shoaling and by $\tilde{t} = 18.0$, is $\approx 10^{-3}$ at $\Delta\tilde{x} \approx 0$, still small overall relative to $\Delta\tilde{p}$ in the lee, but of the same magnitude as $\Delta\tilde{p}$ at $\Delta\tilde{x} \approx 0$ for $\text{Re}^* = 2400$ (figure 9i,j). Thus, surface tension effects are generally small but not negligible relative to pressure. Relative to the residual \tilde{R} , because \tilde{T} is concentrated where \tilde{R} is concentrated, the surface tension term is orders of magnitude smaller than \tilde{R} for $\tilde{t} \leq 18.0$. As the overturning jet forms and falls, then surface tension effects will become even more important.

4. Discussion of wind effects on the solitary wave

4.1. Wave shoaling

We now discuss the wind effects on wave shoaling statistics (figure 4) in the context of previous studies. Zdyrski & Feddersen (2022) derived a vKdV-Burgers equation for soliton shoaling over mildly sloping bathymetry with Jeffrey's style wind forcing (Jeffreys 1925) where the air-water interface pressure is proportional to $\partial\eta/\partial x$. This equation only applies asymptotically well before wave overturning. Although their slope was $3\text{--}7\times$ gentler than that here, for offshore to onshore

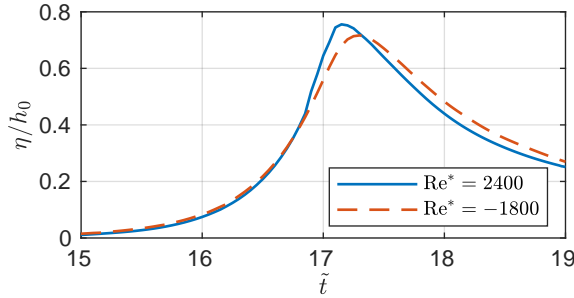


Figure 10. Air-water interface height η/h_0 versus \tilde{t} at location $x/h_0 = 37.5$ for $\text{Re}^* = 2400$ and $\text{Re}^* = -1800$.

577 wind, their wind-forced solitary wave had qualitatively similar shoaling to those here, particularly
 578 the steepness of the front of the wave (figure 4d). This similarity occurs even though the air-water
 579 interface pressure distribution only has a loose qualitative resemblance to the Jeffrey's style wind
 580 forcing. The effect of wind on the solitary wave during shoaling is also qualitatively similar to the
 581 laboratory experiments with periodic waves and wind with U/C varying from 0 to 6 (Feddersen
 582 & Veron 2005). At a fixed location, the time evolution of the shoaling wave revealed a larger
 583 maximum elevation and a temporally-narrower wave than for no wind. Similar features were seen
 584 in the solutions of Zdyrski & Feddersen (2022) for onshore and offshore wind. Here, we examine
 585 the temporal evolution of η/h_0 at a location of $x/h_0 = 37.5$ that is still on the bathymetric slope
 586 but that has shallowed significantly (figure 10). At this virtual wave gauge, the solitary wave
 587 has shoaled significantly. At this location, the $\text{Re}^* = 2400$ solitary wave reaches a maximum
 588 $\eta/h_0 = 0.76$ at $\tilde{t} = 17.15$ and decays rapidly (blue curve in Figure 10). The $\text{Re}^* = -1800$ solitary
 589 wave initially increases similarly to the $\text{Re}^* = 2400$ until $\eta/h_0 = 0.4$ (orange dashed in figure 10).
 590 The subsequent maximum $\eta/h_0 = 0.73$ is smaller and shifted slightly later in time. The subsequent
 591 temporal decay is also shifted later such that the temporal width of the solitary wave is wider
 592 for $\text{Re}^* = -1800$. This is qualitatively similar to the laboratory experiments (Feddersen & Veron
 593 2005) and that of the relatively simple vKdV-Burgers equation (Zdyrski & Feddersen 2022) even
 594 accounting for differences in wind forcing, bathymetry, and periodic versus solitary waves.

595

4.2. Wave overturning

596 The integrated wind-induced surface pressure effect on the shoaling solitary wave then leads to
 597 differences in the breakpoint location and the overturn geometrical parameters (figures 6,7). The
 598 geometrical parameters in the present numerical simulations have similarities and differences to the
 599 field-scale experiment of Feddersen *et al.* (2023). The breakpoint location $\Delta x/h_0$ and overturn area
 600 A_o/H_b^2 (figure 7a,c) have similar functional dependence on wind to the field-scale observations.
 601 However, the aspect ratio W/L (figure 7d) did not. Furthermore, variation in overturn geometrical
 602 parameters require a stronger wind in the present simulations than in the field-scale observations.
 603 Here we explore potential causes for these differences.

604 4.2.1. Wave Reynolds number and Bond number effects

605 The $\text{Re}_w = 4 \times 10^4$ and $\text{Bo} = 4000$ values in this study are much smaller than the field-scale
 606 values ($\text{Re}_w = 1.4 \times 10^7$ and $\text{Bo} = 3.6 \times 10^5$) of Feddersen *et al.* (2023) as both Re_w and Bo are
 607 defined in terms of the offshore depth h_0 . The wave energy decreases marginally but noticeably
 608 for all Re^* (Figure 4c). As expected, for strongest offshore wind ($\text{Re}^* = -1800$), the wave energy
 609 decrease is most noticeable, decreasing 2% from $\tilde{t} = 11$ to 18. Even the strongest onshore wind
 610 case $\text{Re}^* = 2400$, shows wave energy loss. This indicates that the pressure work of the wind on
 611 the solitary wave is relatively weak. BEM-based potential-flow models simulate well with with

612 near-perfect energy conservations laboratory solitary waves that propagate long-distances without
 613 significant dissipation (Grilli *et al.* 1994). Such BEM models are in the $\text{Re}_w \rightarrow \infty$ regime. Here,
 614 we our Re_w is finite and the weak energy decrease across all Re^* is likely due to viscous dissipation
 615 at the bottom and air-water interface boundary layers. The boundary layers have thicknesses
 616 proportional to $\text{Re}_w^{-1/2}$ (Batchelor 1967) which result in an exponential wave height decrease with
 617 decay constant also proportional to $\text{Re}_w^{-1/2}$ (Keulegan 1948). The present Re_w being much smaller
 618 than field values results in more dissipation in the shoaling wave prior to breaking. This may then
 619 indirectly require a stronger $\langle U \rangle / C$ than in the field in order to generate the same geometrical
 620 overturn parameters.

621 Any Bo effects are strongest at overturning when interface curvature is largest. For deep-water
 622 breaking Stokes waves, Mostert *et al.* (2022) observed that Bo did not affect the nonlinear
 623 steepening processes, but directly modulated the geometrical overturn parameters. That study did
 624 identify a sufficiently large Bo (defined according to the deep-water breaker wavelength, hence
 625 different from the definition here) for which surface tension effects ceased to affect the overturn.
 626 That the surface tension contribution reaches the same order as pressure contribution in the surface
 627 dynamic boundary condition (Figure 9i,j), implies that surface tension effects are not negligible
 628 during overturning, and therefore could have some effect on the overturn geometry, potentially
 629 explaining the different aspect ratio relationship to wind between the present simulations and the
 630 field experiment. Quantifying potential Re_w and Bo effects is left for future work.

631 4.2.2. Two dimensional versus three dimensional turbulence

632 Two-dimensional simulations are convenient with lower computational cost. They provide a
 633 good indication of energetic dissipation during wave breaking, as discussed by Iafrati (2009);
 634 Deike *et al.* (2015); Mostert *et al.* (2022) in the context of deep water breakers. However, here we
 635 are concerned with the wind-induced effects on steepening and overturning solitary wave, which
 636 depends on the structure of the airflow over the air-water interface. An obvious 2D effect in the
 637 present simulations is the formation of relatively large, wake vortices for both onshore and offshore
 638 wind (Figures 3, 5). This air turbulence is constrained to be 2D and and therefore characterized by
 639 an inverse energy cascade transferring energy from smaller to larger scales. This is in contrast to
 640 the 3D turbulent airflow in the field-scale experiment of Feddersen *et al.* (2023), featuring a direct
 641 cascade where larger eddies rapidly break up to smaller scales. The air-flow separation, wake,
 642 and reattachment to the solitary wave during wave shoaling would be different between 2D and
 643 3D turbulence, and certainly result in different pressure forcing at the air-water interface. More
 644 concretely, for strong onshore wind ($\text{Re}^* = 2400$, figure 3a,c), the airflow wake has scales of the
 645 solitary wave height, and flow reattachment occurs many x/h_0 in front of the wave. This results in
 646 a wake low pressure that is much broader than for offshore wind (figure 9g,h). If the turbulent
 647 were 3D, flow reattachment would likely occur closer to the wave with the wake low pressure
 648 region being thus narrower, and particularly for onshore wind, affecting more the wave face. As
 649 overturning begins, the wake structure would also be different. With the associated different
 650 air-water interface pressure, the resulting overturn geometry would likely be different. This may
 651 explain the qualitatively different W/L dependence on wind between simulations (figure 6d) and
 652 field experiment as well as simulations requiring a stronger $\langle \bar{U} \rangle / C$.

653 4.2.3. Two versus three dimensional wave overturning

654 The present simulations and the field study of Feddersen *et al.* (2023) have underlying geometrical
 655 differences in wave overturning. In our simulations, the wave overturn is 2D (e.g. figure 5) which
 656 can be interpreted as an overturn with infinitely long crest, the entirety of which is simultaneously
 657 overturning. However, the solitary wave at the Surf Ranch (Feddersen *et al.* 2023) approaches
 658 shore obliquely and overturns progressively (figure 11) such that wave overturning is 3D, with
 659 significant along-crest variation. The wave transitions along-crest from an offshore region where

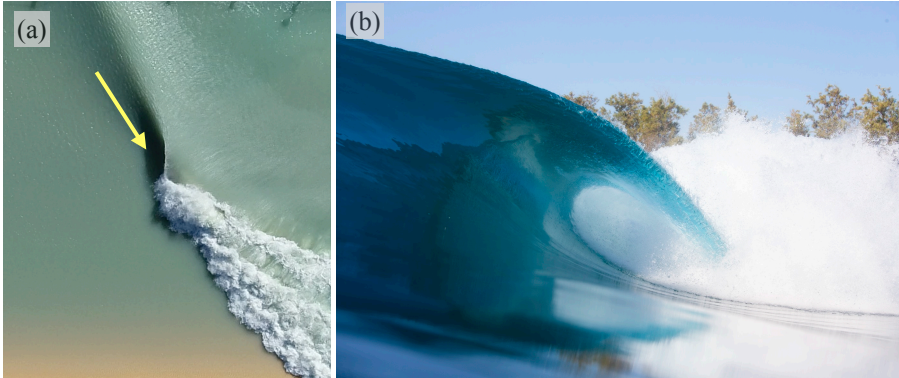


Figure 11. Photos of progressively shoaling and overturning solitary waves at the Surf Ranch: (a) Aerial photo of the obliquely incident solitary wave with arrow indicating a view into the overturn and (b) photo looking into the progressively overturning solitary wave. Note the two photos are of different waves. Progressively overturning waves are the norm in the ocean. Photo credits: (a) Rob Grenzbeck, (b) Pat Stacey.

660 η is single valued, through the process of overturning, ending in a region where the overturn
 661 void collapses and only foam is present (figure 11). Most depth-limited wave breaking in the
 662 ocean is 3D. The geometrical differences between 2D and 3D overturning likely result in different
 663 pressure distributions during overturning. For a 2D overturn, the moment of impact leads to a
 664 dramatic increase in air pressure ($\bar{p} = 0.08$) trapped by the water of the overturn (figure 12). This
 665 \bar{p} magnitude is $20\times$ to $40\times$ larger than that during shoaling (figure 9). In contrast, a progressive
 666 3D overturn (as in Feddersen *et al.* 2023) always has an overturn volume open to one spanwise
 667 side, inducing a spanwise airflow out of the overturn. This would lead to a pressure drop within the
 668 overturn, which is not captured in our 2D simulations. The resulting air-water pressure distribution
 669 would be different during the overturning. This may explain the differences seen between the 3D
 670 overturning (Feddersen *et al.* 2023) and the simulated 2D overturning, particularly in the aspect
 671 ratio W/L .

672 Lastly, we note that the rounded shape of the tip of the plunging jet in figure 12 is consistent
 673 with a range of prior studies. High-resolution DNS of 2D solitary waves, showed a plunging
 674 solitary wave with a round tip (e.g. figure 6 of Mostert & Deike 2020). A similar feature is seen in
 675 in the fully nonlinear potential flow simulations (e.g. figure 4 of Grilli *et al.* 1997). Such rounded
 676 jet tips were observed in laboratory experiments of overturning solitary waves (Li & Raichlen
 677 2003). The rounded jet tip is consistent with experimental deep water plunging waves (Erinin *et al.*
 678 2023*b,a*). A rounded jet tip is also evident in the image in Figure 11b.

679 4.3. Implications and the overturning jet

680 The implications of the wind effects on overturned shoaling and overturning waves was discussed
 681 in Feddersen *et al.* (2023). Essentially onshore and offshore wind for the otherwise identical
 682 wave field will induce changes to wave overturning shape generating different cross-shore wave
 683 dissipation patterns, turbulence injection, and sediment suspension. Such effects are not accounted
 684 for in modern coastal engineering wave models. Such wind-induced effects, may then eventually
 685 affect nearshore morphological evolution. Potential wind effects on turbulence injection can be
 686 concretely seen in the modeled overturning jet area A_J/H_b^2 (figure 7e), whose wind effects have
 687 not been examined previously. Spanning the strongest offshore to onshore wind, A_J/H_b^2 varies by a
 688 factor of two, the strongest variation in all the parameters. This A_J/H_b^2 variation also equates to a
 689 large variations in potential energy available in the overturn. This will lead to stronger turbulence

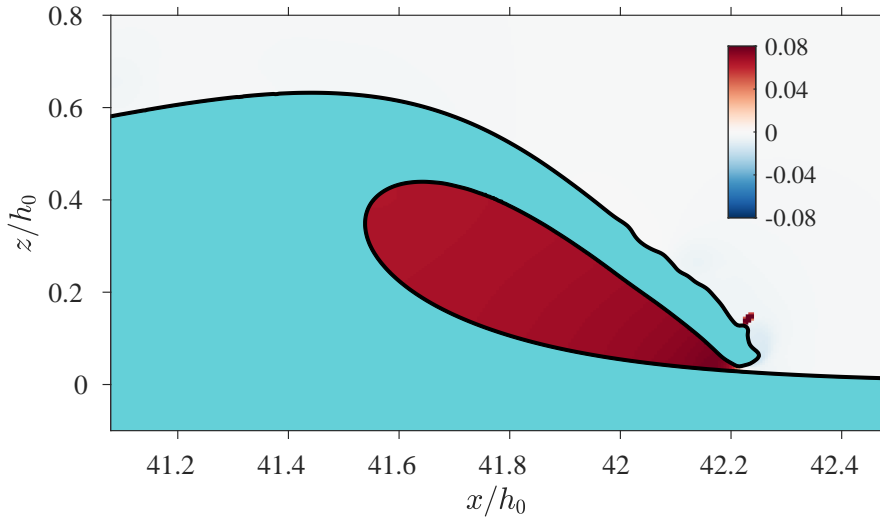


Figure 12. For $Re^* = -1800$ at $\tilde{t} = 20.22$, overturning solitary wave (aqua blue) at the moment of overturning jet impact on the water surface with overlaid air pressure as a function of horizontal x/h_0 and vertical z/h_0 coordinates. The air-water interface is indicated by the black curve. Note the very high pressure within the nearly enclosed overturn.

690 injection and increased sediment suspension near the breakpoint for offshore wind relative to
 691 onshore wind. Such wind-effects are commonly understood in the surfing community.

692 5. Summary

693 Here wind effects (given by the wind Reynolds number Re^*) on solitary wave shoaling and
 694 overturning were studied with the 2-phase DNS model Basilisk run in two-dimensions. The
 695 fixed bathymetry was similar to that of the Surf Ranch. Wave Reynolds and Bond numbers
 696 ($Re_w = 4 \times 10^4$, $Bo = 4000$) were fixed, at values orders of magnitude smaller than experiment.
 697 A precursor wind-only simulation (Appendix A) provides wind initial condition. During the
 698 subsequent 2-phase simulations, wind forcing is removed, but the wind does not have sufficient
 699 time to meaningfully decelerate (Appendix B). The propagating solitary wave sheds a 2D turbulent
 700 air wake either in front of the wave for onshore wind or on the back of the wave for offshore wind.
 701 The onshore and offshore wind cases have different wake structure. The propagating solitary wave
 702 has nearly uniform speed with minimal wind-induced energy changes over the rapidly varying
 703 bathymetry for all Re^* . The solitary wave face slope is clearly influenced by the wind, with
 704 steeper slope for stronger onshore wind. Changes to modeled shoaling solitary wave shape are
 705 qualitatively consistent with previous laboratory studies and reduced order models. At the moment
 706 of overturning jet impact, wind-dependent differences in overturn wave shape are evident and these
 707 shapes are quantified by geometrical parameters. The nondimensional breakpoint location and
 708 overturn area have similar functional dependence on wind as in experiment. However, modeled
 709 wind speeds that are a factor 2–3 stronger than observed are required. The overturn aspect ratio
 710 had opposite functional dependence on wind than in experiment. The overturning jet area, not
 711 having been previously studied, depends strongly on wind. Airflow can affect the water-based
 712 solitary wave through two mechanisms on the air-water interface: pressure or viscous stresses.
 713 Throughout the shoaling processes normal and shear viscous stresses are negligible relative to
 714 pressure on the air-water interface. Surface tension effects are negligible early in shoaling, but as
 715 the wave steepens these effects grow rapidly such that near overturning, surface tension effects are
 716 no longer negligible and likely become important in overturning. In a propagating solitary wave

717 frame of reference, pressure is low in the lee and contributes 2-5% to the velocity potential rate
 718 of change in the surface dynamic boundary condition. Integrated over the time of shoaling, this
 719 leads to changes in the wave shape. Although at far smaller Re_w and Bo , wind-induced changes to
 720 modeled shoaling and overturning wave shape are largely consistent with wind-effects seen in
 721 previous laboratory (Feddersen & Veron 2005) and field-scale (Feddersen *et al.* 2023) studies.
 722 Three potential reasons why the modeled overturn aspect ratio differs from experiment and why a
 723 stronger modeled wind is required are explored. The first involves potential scale effects resulting
 724 from our Re_w and Bo being much smaller than field-scale. The second is that the airflow is 2D
 725 rather than not 3D, resulting in different flow separation, wake structure, and reattachment than
 726 experiment. The third is an underlying difference in the modeled 2D geometry of wave breaking
 727 relative to the 3D geometry at the Surf Ranch. This study with a 2D model configuration is
 728 the first computational study to examine in detail the effect of wind on shoaling and overturning
 729 wave shape. The dramatic wind-effects on the nondimensional overturning jet area, and thus to
 730 the potential energy available in the overturn, make concrete the implications of wind-induced
 731 changes to wave shape. However, new questions have also been raised, and addressing them will
 732 necessitate 3D simulations at far greater computational cost.

733 **Acknowledgments** We are grateful to the Mark Walk Wolfinger Surfzone Processes Research
 734 Fund who provided support to make this research possible. We thank the World Surf League and
 735 the Kelly Slater Wave Company for their support of this work. Discussions with Chris Blenkinsopp,
 736 Marc Buckley, and Mark McAllister provided useful insight.

737 **Funding.** The Mark Walk Wolfinger Surfzone Processes Research Fund supported this research at
 738 Scripps Institution of Oceanography.

739 **Declaration of Interests.** The authors report no conflict of interest.

740 **Data Availability Statement.** Basilisk code used run the model and to perform data analysis in
 741 this study can be found at <http://basilisk.fr/sandbox/ffeddersen/> MATLAB analysis code can be
 742 found at <https://zenodo.org/doi/10.5281/zenodo.13351600>

743 **Author ORCID.** Falk Feddersen, <https://orcid.org/0000-0002-5488-9074>; Kentaro Hanson,
 744 <https://orcid.org/0000-0002-0468-226X>; Wouter Mostert, <https://orcid.org/0000-0001-6251-4136>;

745 **Appendix A. Precursor simulations to obtain wind air initial condition**

746 An air-only simulation over a moving solitary wave solid boundary is performed as a precursor
 747 to each coupled simulation, providing air initial conditions to the coupled model. The precursor
 748 simulation is done under a Galilean transformation in the reference frame of the solitary wave, and
 749 is physically equivalent to allowing an unchanging solitary wave to propagate in an arbitrarily
 750 long channel of constant depth in the presence of wind. At the solitary wave surface, a no-slip
 751 velocity boundary condition given by (2.4) and translated through a Galilean transformation into
 752 the solitary wave's frame of reference moving at \bar{C} in the $+x$ direction is applied. In the solitary
 753 wave reference frame, air-flow at the air-water interface must be in the $-x$ direction to match the
 754 solitary wave surface velocity boundary conditions (2.4). An external, spatially, and temporally
 755 uniform pressure gradient is used to force the wind given by (2.8). The precursor simulation is
 756 run until equilibrium. The equilibrium airflow is relatively insensitive to the choice of initial
 757 condition, which affects only the time to equilibrate. Here, the initial condition for air vertical
 758 velocity is $w = 0$. The initial condition for horizontal velocity is uniform in x and u is set to a
 759 logarithmic profile transformed into the solitary wave reference frame with an inner-layer velocity
 760 profile that goes to $u = -C$ at the boundary. This u initial condition does not match the no-slip
 761 boundary condition on the solitary wave (2.4). However any generated transients are advected

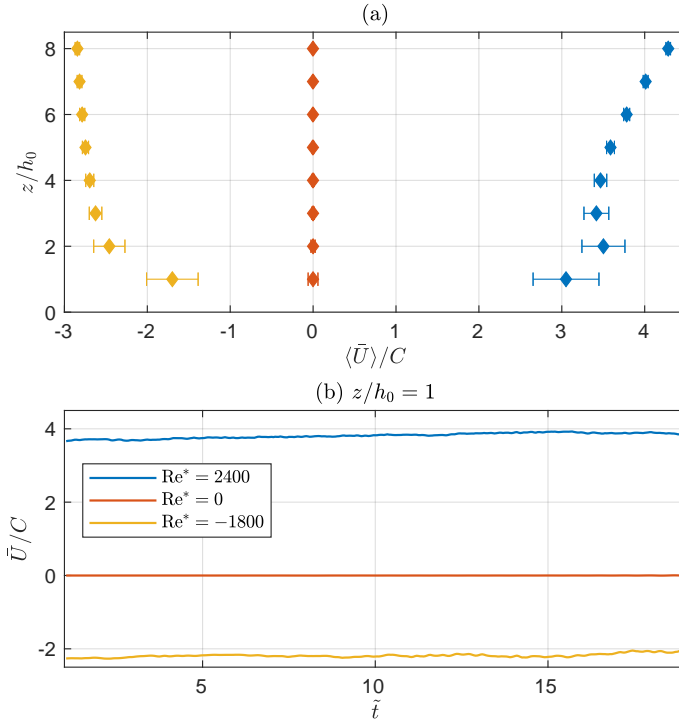


Figure 13. (a) Nondimensional mean wind speed $\langle \bar{U} \rangle / C$ profiles as a function of z/h_0 for three Re^* with horizontal bars indicating both time and horizontal standard deviation. (b) Time series of x -averaged nondimensional wind speed \bar{U} / C as a function of nondimensional time $\bar{t} = t(g/h_0)^{1/2}$ for three Re^* . The legend in (b) also applies to (a).

762 way, eventually leaving an equilibrated state for use as initial condition in the coupled air-water
 763 simulations. Identical to the coupled simulation, Neumann pressure condition $\partial p / \partial x = 0$ is placed
 764 on the inlet and a Dirichlet pressure condition $p = 0$ is placed on the outlet, both uniformly
 765 in the vertical. In the moving reference frame, the air-flow in the precursor stage may not be
 766 unidirectional, particularly for strong onshore winds as the near-surface airflow will be in the $-x$
 767 direction and higher in the air column will be in the $+x$ direction and thus neither boundary is fully
 768 an inlet or outlet. However, since the airflow is forced and the solitary wave is sufficiently far from
 769 either boundary, specific choices for lateral boundary conditions do not significantly affect the
 770 wind profile. For all Re^* , the precursor simulations were performed for a nondimensional runtime
 771 ($\Delta \bar{t}$) of 1000 with a maximum of 11 levels of grid refinement resulting in $\Delta x / h_0 = 0.0293$ which
 772 is sufficient, due to the relatively large-scale of the solitary wave and the lack of need to resolve
 773 very small-scale dynamics such as the overturn. A nondimensional runtime of 800 was sufficient
 774 for obtaining an equilibrated initial condition for the largest Re^* magnitude.

775 Appendix B. Wind statistics during the shoaling stage

776 Here, we provide statistics of the wind velocity during the shoaling stage. The x -averaged
 777 non-dimensional wind speed is given by $\bar{U}(z, t) / C$ (2.13) and the time-average of \bar{U} / C is $\langle \bar{U} \rangle(z) / C$

778 (2.14). The standard deviation σ_U represents both time and horizontal variability and is given by

$$\sigma_U(z/h_0) = \left[\frac{1}{18} \int_1^{19} \left\{ \frac{1}{L_x/h_0} \int_0^{L_x/h_0} [u(x/h_0, z/h_0, \tilde{t}) - \langle \bar{U} \rangle(z/h_0)]^2 d(x/h_0) \right\} d\tilde{t} \right]^{1/2}. \quad (\text{B } 1)$$

779 For $\text{Re}^* = 0$, $\langle \bar{U} \rangle/C$ is essentially zero for all z/h_0 with slight wind variation σ_U/C at $z/h_0 = 1$
 780 (diamonds and horizontal bars in Figure 13a). For onshore or offshore wind ($\text{Re}^* \neq 0$), $\langle \bar{U} \rangle/C$
 781 magnitude mostly increases in the vertical with weak wind variation for $z/h_0 \geq 6$ but with
 782 significant σ_U/C near $z/h_0 = 1$ due to the flow separation off of the solitary wave (Figures 3 &
 783 5). In the reference frame of the moving solitary wave, the wind variability is much weaker. We
 784 also examine the time-dependence of the x -averaged wind velocity \bar{U}/C at the vertical location
 785 of $z/h_0 = 1$ over $1 \leq \tilde{t} \leq 20$ (Figure 13b). For $\text{Re}^* = 0$, the \bar{U}/C is essentially zero for all \tilde{t} . For
 786 onshore wind ($\text{Re}^* = 2400$), \bar{U}/C weakly increases from $\bar{U}/C = 3.67$ at $\tilde{t} = 1$ to $\bar{U}/C = 3.85$
 787 at $\tilde{t} = 19$ as the soliton wake becomes more established. For offshore wind $\text{Re}^* = -1800$, the
 788 wind slows about 10% over the simulation with $\bar{U}/C = -2.25$ at $\tilde{t} = 1$ to $\bar{U}/C = -2.05$ at $\tilde{t} = 19$.
 789 Overall these 10% variations in \bar{U}/C indicate that, with the forcing turned off, the wind is largely
 790 steady over the time of shoaling and commencement of overturning.

REFERENCES

- 791 AAGAARD, TROELS, HUGHES, MICHAEL G. & RUESSINK, GERBEN 2018 Field observations of turbulence, sand
 792 suspension, and cross-shore transport under spilling and plunging breakers. *Journal of Geophysical*
 793 *Research: Earth Surface* **123** (11), 2844–2862.
- 794 ABLOWITZ, MARK J. 2011 *Nonlinear Dispersive Waves: Asymptotic Analysis and Solitons*. Cambridge
 795 University Press.
- 796 BATCHELOR, GEORGE KEITH 1967 *An introduction to fluid dynamics*. Cambridge university press.
- 797 BELL, JOHN B, COLELLA, PHILLIP & GLAZ, HARLAND M 1989 A second-order projection method for the
 798 incompressible Navier-Stokes equations. *Journal of Computational Physics* **85** (2), 257–283.
- 799 BLENKINSOPP, C.E & CHAPLIN, J.R 2007 Void fraction measurements in breaking waves. *Proceedings of the*
 800 *Royal Society A: Mathematical, Physical and Engineering Sciences* **463** (2088), 3151–3170.
- 801 BLENKINSOPP, C.E. & CHAPLIN, J.R. 2008 The effect of relative crest submergence on wave breaking over
 802 submerged slopes. *Coastal Engineering* **55** (12), 967–974.
- 803 BOSWELL, HUNTER, YAN, GUIRONG & MOSTERT, WOUTER 2023 Characterizing energy dissipation of
 804 shallow-water wave breaking in a storm surge. *Phys. Rev. Fluids* **8**, 054801.
- 805 BRACKBILL, J.U, KOTHE, D.B & ZEMACH, C 1992 A continuum method for modeling surface tension. *Journal*
 806 *of Computational Physics* **100** (2), 335–354.
- 807 BULLOCK, G.N., OBHRAI, C., PEREGRINE, D.H. & BREDMOSE, H. 2007 Violent breaking wave impacts. part 1:
 808 Results from large-scale regular wave tests on vertical and sloping walls. *Coastal Engineering* **54** (8),
 809 602–617.
- 810 CHANSON, HUBERT & JAW-FANG, LEE 1997 Plunging jet characteristics of plunging breakers. *Coastal*
 811 *Engineering* **31** (1), 125–141.
- 812 CHEN, GANG, KHARIF, CHRISTIAN, ZALESKI, STÉPHANE & LI, JIE 1999 Two-dimensional Navier–Stokes
 813 simulation of breaking waves. *Physics of Fluids* **11** (1), 121–133.
- 814 CHEN, HAIFEI & ZOU, QINGPING 2022 Geometry of deep and intermediate water breaking waves influenced
 815 by wind speed and direction. *Physics of Fluids* **34** (8), 087126.
- 816 CHEN, JINSHI, RAUBENHEIMER, BRITT & ELGAR, STEVE 2024 Wave and roller transformation over barred
 817 bathymetry. *Journal of Geophysical Research: Oceans* **129** (5), e2023JC020413.
- 818 DEIKE, LUC, MELVILLE, W KENDALL & POPINET, STÉPHANE 2016 Air entrainment and bubble statistics in
 819 breaking waves. *Journal of Fluid Mechanics* **801**, 91–129.
- 820 DEIKE, LUC, POPINET, STEPHANE & MELVILLE, W 2015 Capillary effects on wave breaking. *Journal of Fluid*
 821 *Mechanics* **769**, 541–569.
- 822 DERAKHTI, MORTEZA & KIRBY, JAMES T. 2014 Bubble entrainment and liquid–bubble interaction under
 823 unsteady breaking waves. *Journal of Fluid Mechanics* **761**, 464–506.

- 824 DOUGLASS, SCOTT L 1990 Influence of wind on breaking waves. *J. Waterw. Port Coast. Ocean Eng.* **116** (6),
825 651–663.
- 826 ELGAR, STEVE & GUZA, R T 1985 Observations of bispectra of shoaling surface gravity waves. *J. Fluid Mech.*
827 **161**, 425–448.
- 828 ERININ, MARTIN A, LIU, CHANG, WANG, SOPHIE D, LIU, XINAN & DUNCAN, JAMES H 2023a Plunging
829 breakers. part 2. droplet generation. *Journal of Fluid Mechanics* **967**, A36.
- 830 ERININ, MARTIN A, LIU, XINAN, WANG, SOPHIE D & DUNCAN, JAMES H 2023b Plunging breakers. part 1.
831 analysis of an ensemble of wave profiles. *Journal of Fluid Mechanics* **967**, A35.
- 832 FEDDERSEN, FALK, FINCHAM, ADAM M., BRODIE, KATHERINE L., YOUNG, ADAM P., SPYDELL, M.S., GRIMES,
833 DEREK J., PIESZKA, MICHAL & HANSON, KENTARO 2023 Cross-shore wind-induced changes to
834 field-scale overturning wave shape. *Journal of Fluid Mechanics* **958**, A4.
- 835 FEDDERSEN, FALK & VERON, FABRICE 2005 Wind effects on shoaling wave shape. *J. Phys. Oceanogr.* **35** (7),
836 1223–1228.
- 837 FUSTER, DANIEL & POPINET, STÉPHANE 2018 An all-mach method for the simulation of bubble dynamics
838 problems in the presence of surface tension. *Journal of Computational Physics* **374**.
- 839 GREEN, ALBERT EDWARD, LAWS, N & NAGHDI, PM 1974 On the theory of water waves. *Proceedings of the*
840 *Royal Society of London. A. Mathematical and Physical Sciences* **338** (1612), 43–55.
- 841 GRILLI, S. T., SUBRAMANYA, R., SVENDSEN, I. A. & VEERAMONY, J. 1994 Shoaling of solitary waves on plane
842 beaches. *Journal of Waterway, Port, Coastal, and Ocean Engineering* **120** (6), 609–628.
- 843 GRILLI, STEPHAN T, SVENDSEN, IB A & SUBRAMANYA, RAVISHANKAR 1997 Breaking criterion and
844 characteristics for solitary waves on slopes. *J. Waterw. Port Coast. Ocean Eng.* **123** (3), 102–112.
- 845 GUIGNARD, STEPHAN, MARCER, RICHARD, REY, VINCENT, KHARIF, CHRISTIAN & FRAUNIE, PHILIPPE 2001
846 Solitary wave breaking on sloping beaches: 2-d two phase flow numerical simulation by sl-vof method.
847 *European Journal of Mechanics - B/Fluids* **20** (1), 57–74.
- 848 GUYENNE, P. & GRILLI, S. T. 2006 Numerical study of three-dimensional overturning waves in shallow water.
849 *Journal of Fluid Mechanics* **547**, 361–388.
- 850 HAO, XUANTING & SHEN, LIAN 2019 Wind–wave coupling study using les of wind and phase-resolved
851 simulation of nonlinear waves. *Journal of Fluid Mechanics* **874**, 391–425.
- 852 VAN HOOFT, J. ANTOON, POPINET, STÉPHANE, VAN HEERWAARDEN, CHIEL C., VAN DER LINDEN, STEVEN J. A.,
853 DE ROODE, STEPHAN R. & VAN DE WIEL, BAS J. H. 2018 Towards adaptive grids for atmospheric
854 boundary-layer simulations. *Boundary-Layer Meteorology* **167** (3), 421–443.
- 855 IAFRATI, A 2009 Numerical study of the effects of the breaking intensity on wave breaking flows. *Journal of*
856 *Fluid Mechanics* **622**, 371–411.
- 857 JEFFREYS, HAROLD 1925 On the formation of water waves by wind. *Proc. R. Soc. Lond. A* **107** (742), 189–206.
- 858 JOHANSEN, HANS & COLELLA, PHILLIP 1998 A Cartesian grid embedded boundary method for Poisson’s
859 equation on irregular domains. *Journal of Computational Physics* **147**, 60–85.
- 860 KEULEGAN, GARBIS H 1948 Gradual damping of solitary waves. *J. Res. Natl. Bur. Stand* **40** (6), 487–498.
- 861 KNOWLES, JEFFREY & YEH, HARRY 2018 On shoaling of solitary waves. *J. Fluid Mech.* **848**, 1073–1097.
- 862 LE MÉTAYER, O., GAVRILYUK, S. & HANK, S. 2010 A numerical scheme for the Green–Naghdi model. *Journal*
863 *of Computational Physics* **229** (6), 2034–2045.
- 864 LEYKIN, I A, DONELAN, M A, MELLEN, R H & McLAUGHLIN, D J 1995 Asymmetry of wind waves studied in
865 a laboratory tank. *Nonlinear Process Geophys.* **2** (3/4), 280–289.
- 866 LI, YING & RAICHLEN, FREDRIC 2003 Energy balance model for breaking solitary wave runup. *Journal of*
867 *Waterway, Port, Coastal, and Ocean Engineering* **129** (2), 47–59.
- 868 LIN, PENGZHI & LIU, PHILIP L.-F. 1998 A numerical study of breaking waves in the surf zone. *Journal of*
869 *Fluid Mechanics* **359**, 239–264.
- 870 LIU, SHUO, WANG, HUI, BAYEUL-LAINÉ, ANNIE-CLAUDE, LI, CHENG, KATZ, JOSEPH & COUTIER-DELGOSHA,
871 OLIVIER 2023 Wave statistics and energy dissipation of shallow-water breaking waves in a tank with a
872 level bottom. *Journal of Fluid Mechanics* **975**, A25.
- 873 LONGUET-HIGGINS, M. S. 1982 Parametric solutions for breaking waves. *Journal of Fluid Mechanics* p.
874 403–424.
- 875 LUBIN, P. & GLOCKNER, S. 2015 Numerical simulations of three-dimensional plunging breaking waves:
876 Generation and evolution of aerated vortex filaments. *Journal of Fluid Mechanics* **767**, 364–393.
- 877 LUBIN, PIERRE, KIMMOUN, OLIVIER, VÉRON, FABRICE & GLOCKNER, STÉPHANE 2019 Discussion on instabilities
878 in breaking waves: vortices, air-entrainment and droplet generation. *European Journal of Mechanics-*
879 *B/Fluids* **73**, 144–156.
- 880 LUBIN, PIERRE, VINCENT, STÉPHANE, ABADIE, STÉPHANE & CALTAGIRONE, JEAN-PAUL 2006 Three-dimensional

- 881 large eddy simulation of air entrainment under plunging breaking waves. *Coastal Engineering* **53** (8),
882 631–655.
- 883 LÓPEZ-HERRERA, J.M., POPINET, S. & CASTREJÓN-PITA, A.A. 2019 An adaptive solver for viscoelastic
884 incompressible two-phase problems applied to the study of the splashing of weakly viscoelastic
885 droplets. *Journal of Non-Newtonian Fluid Mechanics* **264**, 144–158.
- 886 MILES, JOHN W 1957 On the generation of surface waves by shear flows. *J. Fluid Mech.* **3** (2), 185–204.
- 887 MOSTERT, WOUTER & DEIKE, LUC 2020 Inertial energy dissipation in shallow-water breaking waves. *J. Fluid*
888 *Mech.* **890**, A12.
- 889 MOSTERT, W., POPINET, S. & DEIKE, L. 2022 High-resolution direct simulation of deep water breaking waves:
890 transition to turbulence, bubbles and droplets production. *Journal of Fluid Mechanics* **942**, A27.
- 891 O'DEA, ANNIKA, BRODIE, KATHERINE & ELGAR, STEVE 2021 Field observations of the evolution of
892 plunging-wave shapes. *Geophysical Research Letters* **48** (16), e2021GL093664.
- 893 PEREGRINE, D H 1983 Breaking waves on beaches. *Annual Review of Fluid Mechanics* **15** (1), 149–178.
- 894 PHILLIPS, OWEN M 1957 On the generation of waves by turbulent wind. *J. Fluid Mech.* **2** (5), 417–445.
- 895 POPINET, STÉPHANE 2003 Gerris: a tree-based adaptive solver for the incompressible euler equations in
896 complex geometries. *Journal of Computational Physics* **190** (2), 572–600.
- 897 POPINET, STÉPHANE 2009 An accurate adaptive solver for surface-tension-driven interfacial flows. *Journal of*
898 *Computational Physics* **228**, 5838–5866.
- 899 POPINET, STÉPHANE 2018 Numerical models of surface tension. *Annual Review of Fluid Mechanics* **50** (1),
900 49–75, arXiv: <https://doi.org/10.1146/annurev-fluid-122316-045034>.
- 901 SOUS, DAMIEN, FORSBERG, PERNILLE LOUISE, TOUBOUL, JULIEN & GONÇALVES NOGUEIRA, GUILHERME 2021
902 Laboratory experiments of surf zone dynamics under on- and offshore wind conditions. *Coastal*
903 *Engineering* **163**, 103797.
- 904 TANAKA, MITSUHIRO 1986 The stability of solitary waves. *The Physics of Fluids* **29** (3), 650–655.
- 905 TING, F. C. K. & KIRBY, J. T. 1995 Dynamics of surf-zone turbulence in a strong plunging breaker. *Coastal*
906 *Engineering* **24** (3-4), 177–204.
- 907 TING, F C K & KIRBY, J T 1996 Dynamics of surf-zone turbulence in a spilling breaker. *Coastal Engineering*
908 **27** (3-4), 131–160.
- 909 WEI, GE, KIRBY, JAMES T., GRILLI, STEPHAN T. & SUBRAMANYA, RAVISHANKAR 1995 A fully nonlinear
910 boussinesq model for surface waves. part 1. highly nonlinear unsteady waves. *Journal of Fluid*
911 *Mechanics* **294**, 71–92.
- 912 WRONISZIEWSKI, PAWEŁ A, VERSCHAEVE, JORIS CG & PEDERSEN, GEIR K 2014 Benchmarking of Navier–
913 Stokes codes for free surface simulations by means of a solitary wave. *Coastal Engineering* **91**,
914 1–17.
- 915 WU, JIARONG & DEIKE, LUC 2021 Wind wave growth in the viscous regime. *Phys. Rev. Fluids* **6**, 094801.
- 916 WU, JIARONG, POPINET, STÉPHANE & DEIKE, LUC 2022 Revisiting wind wave growth with fully coupled direct
917 numerical simulations. *Journal of Fluid Mechanics* **951**, A18.
- 918 XIE, ZHIHUA 2014 Numerical modelling of wind effects on breaking solitary waves. *Eur. J. Mech. B Fluids*
919 **43**, 135–147.
- 920 XIE, ZHIHUA 2017 Numerical modelling of wind effects on breaking waves in the surf zone. *Ocean Dyn.*
921 **67** (10), 1251–1261.
- 922 YASUDA, TAKASHI, MUTSUDA, HIDEMI, MIZUTANI, NATSUKI & MATSUDA, HIROFUMI 1999 Relationships
923 of plunging jet size to kinematics of breaking waves with spray and entrained air bubbles. *Coastal*
924 *Engineering Journal* **41** (3-4), 269–280.
- 925 ZDYRSKI, THOMAS & FEDDERSEN, FALK 2020 Wind-induced changes to surface gravity wave shape in deep to
926 intermediate water. *J. Fluid Mech.* **903**, A31.
- 927 ZDYRSKI, THOMAS & FEDDERSEN, FALK 2021 Wind-induced changes to surface gravity wave shape in shallow
928 water. *J. Fluid Mech.* **913**, A27.
- 929 ZDYRSKI, THOMAS & FEDDERSEN, FALK 2022 Wind-induced changes to shoaling surface gravity wave shape.
930 *Phys. Rev. Fluids* **7**, 074802.